PREPARATION OF TYPE 2 AND TYPE 3 POROUS LIQUIDS FOR THE ABSORPTION OF VOLATILE ORGANIC COMPOUNDS

BRASCHINSKY, ALAN

PREPARATION OF TYPE 2 AND TYPE 3 POROUS LIQUIDS FOR THE ABSORPTION OF VOLATILE ORGANIC COMPOUNDS

THESIS SUBMITTED IN PARTIAL FULFILLMENT OF THE REQUIREMENTS FOR THE DEGREE OF MASTER OF SCIENCE IN THE DEPARTMENT OF CHEMISTRY

BY

ALAN BRASCHINSKY

DURHAM, UNITED KINGDOM

2020

Table of Contents

Acknowledgments

I would like to thank my supervisor Prof. Jonathan W. Steed for his continuous support and help throughout the period of study. Additionally, I am grateful to the Steed Group for being wonderfully welcoming and creating an environment conducive to learning and discovery.

Abstract

Porous materials have been widely used in various applications from gas capture to electrochemistry. So far, the utilised materials have been of solid phase. However, it has been established that liquid phase materials are more efficient in industrial settings. Thus, engineering accessible porosity into the liquid phase can result in highly efficient and sought-after materials.

The aim of this work was to prepare Type 2 and Type 3 porous liquids for the capture of volatile organic compounds. For the former, dimeric and hexameric nanocapsules were selected due to their relatively small cavity window sizes, which would allow for the encapsulation of small VOCs, yet prevent the entrance of larger solvent molecules. To prepare Type 3 porous liquids, a commercially available Basolite® F300 MOF was selected due to its well-defined pore size and thermal stability. Two types of ionic liquid were employed: imidazolium- and phosphonium-based ionic liquids. Due to the unknown solubility of the porous solids, it was desirable to select both types of IL.

Type 2 porous liquids were not successfully prepared. This was due to the presence of solvent molecules within the cavities of the nanocapsules as evidenced *via* mass spectrometry and NMR spectroscopy and single crystal X-ray diffraction. NMR results showed that the Zn-PgC_3 nanocapsule was incapable of guest exchange. Thus, these nanocapsules were not used for the preparation of Type 2 porous liquids.

On the other hand, stable colloids of Basolite® F300 with the phosphonium-based ILs were prepared. To characterise the presence of empty pores within these colloids, a biphasic dye extraction setup was used and analysed with UV-Vis spectroscopy. The results show that **PL2** does not possess superior dye absorption capabilities compared to its ionic liquid counterpart, indicating that there is no intrinsic porosity within these porous liquids, or that it does not affect dye absorption.

Abbreviations

PL	Porous liquid
IL	Ionic liquid
VOC	Volatile organic compound
MOF	Metal-organic framework
MONC	Metal-organic nanocapsule
DES	Deep eutectic solvent
P-IL	Phosphonium ionic liquid
im-IL	Imidazolium ionic liquid
DMSO	Dimethylsulfoxide
DMF	Dimethylformamide
MeCN	Acetonitrile
MALDI-MS	Matrix-assisted laser desorption/ionization mass spectroscopy
NMR	Nuclear magnetic resonance
DOSY	Diffusion-ordered NMR spectroscopy
SXRD	Single crystal X-ray diffraction
FT-IR	Fourier transform infrared
UV-Vis	Ultraviolet-visible
PXRD	Powder X-ray diffraction
DSC	Differential scanning calorimetry
TGA	Thermogravimetric analysis
HBA	Hydrogen bond acceptor
HBD	Hydrogen bond donor
MFC	Microbial fuel cell
BOD	Biochemical oxygen demand
COD	Chemical oxygen demand
BET	Brunauer-Emmett-Teller
BJH	Barrett-Joyner-Halenda
DFT	Density functional theory
SANS	Small-angle neutron scattering

USANS	Ultra-small-angle neutron scattering
SAXS	Small-angle X-ray scattering
SEM	Scanning electron microscopy
TEM	Transmission electron microscopy
HS	Hollow silica
PEG	(Poly)ethylene glycol
BF300	Basolite® F300
ARS	Alizarin Red S
AB25	Acid Blue 25
NAC	Nitrogen-doped activated carbon

1. Introduction

The presence of porosity in various materials has been widely observed in nature. For example, bamboo, honeycomb, sponges, and soil all contain pores. Porous materials are of significant interest in various applications due to their ability to interact with other compounds not only on their surface but throughout the porous bulk.[1] Such porous materials include zeolites, porous carbon, metal-organic frameworks (MOFs), nanotubes, nanorods and aerogels, along with various polymers. They have found use in many applications in areas such as solar energy systems, gas storage and separation, drug delivery, and crystallisation.[2–5]

Generally, porous materials utilised in such areas are solids. Even though they might be efficient at the desired function, their scale-up and commercialisation can be difficult. For example, post-combustion carbon capture is still mainly performed with amine-based liquids due to their easy manufacture and application.[6] However, these liquids possess many drawbacks, including corrosiveness, which leads to costly implementation and poor recyclability after the end of their lifetime. Thus, the preparation of a benign, easily recycled liquid adsorbent for such applications could significantly improve the effectiveness of current processes.

There are three types of porous liquids (PLs) (Figure 1).[7] Neat liquid hosts incapable of interpenetration are described as Type 1 PLs. Type 2 PLs involve the dissolution of host molecules in a solvent incapable of entering the pores of the host solute. Type 3 PLs are prepared *via* the dissolution of framework-compounds in sterically hindered solvent molecules.

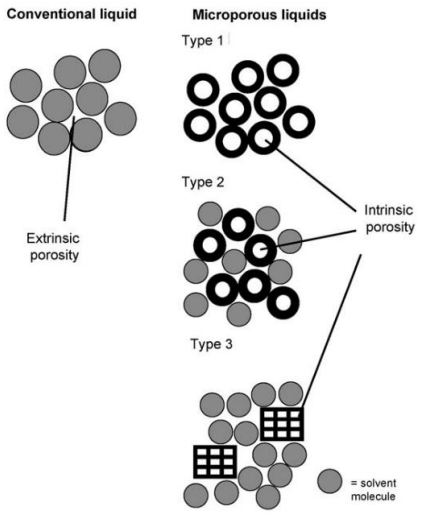

Figure 1: Three types of liquids with permanent porosity. Empty circles represent cage-type compounds and rectangles with empty spaces represent framework-type compounds. Reproduced from ref. 7 with permission

The first example of a permanently porous liquid was reported by James and Cooper.[8] Essentially, a crown ether functionalised amine-based cage (Figure 2) was dissolved in a bulky crown ether solvent. The team found that the presence of a high concentration of empty cages in the solvent resulted in an eightfold increase in the solubility of methane gas compared to the pure crown solvent. While this porous liquid proved to significantly enhance the equilibrium solubility of methane gas, the synthetic route of the cage is very costly and uses volatile solvents that are known to harm the environment. The aim of this work is to prepare a novel porous liquid for the uptake of volatile organic compounds (VOCs) using an environmentally friendly porous liquid.

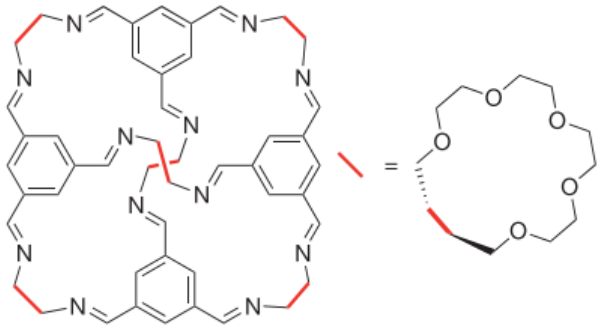

Figure 2: Cage molecule used to prepare a permanently porous liquid by James *et al*. Reproduced from ref. 8 with permission.

1.1 Ionic Liquids

Throughout this work, ionic liquids (ILs) will be denoted as [cation][anion]. For example, in the case of [$C_n$mim][NTf_2], *mim* represents the methyl-imidazolium cation and *n* represents the alkyl chain length off the neutral nitrogen atom. The anion, in this case, is a bistriflimide, also known as bis(trifluoromethanesulfonyl)imide. For example, 1-ethyl-3-methylimidazolium nitrate, as shown in Figure 3, would be denoted as [C_2mim][NO_3]. However, due to the vast number of ILs, it is difficult to formulate a systematic, yet self-consistent naming system for all of them. Thus, in order to avoid confusion, all ILs mentioned in this work will also be accessible in the appendix, with their abbreviations, structures and empirical formulas.

ILs can be classified as salts whose melting point are below 100°C. It is generally accepted that ILs whose melting point lies above this temperature are called molten salts.[9] ILs are composed of a cation and an anion, which means that a plethora of such compounds can be synthesized. In fact, including binary and ternary mixtures, it is estimated that 10^{18} different ILs could be prepared.[10] Interestingly, even though ILs have emerged as very interesting compounds, their history dates back to as far as 1914 when the first IL was synthesised by Walden.[11,12] The first patent related to an IL was granted in 1938, where the use of a molten pyridinium salt at 120°C for water-repellency of cellulosic fibre was described.[13,14] Even though that was almost 90 years ago, research of ILs gained popularity much later, when in the early 1990s the first air and water stable ILs were synthesised.[15] Figure 3 depicts one of the ILs prepared in that study. With the establishment of green chemistry around the same time, ILs became very promising and popular compounds as solvents as they were described as "green" solvents due to their designer properties and nonvolatility.

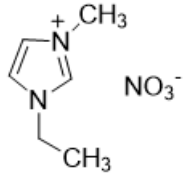

Figure 3: 1-ethyl-3-methylimidazolium nitrate, [C_2mim][NO_3], one of the air and water-stable ionic liquids first reported by Wilkes and Zaworotko.[15]

The research into ILs has grown substantially in recent decades because of their low vapour pressure and low flammability, wide electrochemical window, and high thermal stability.[16,17] They have been labelled "designer solvents", suggesting their properties can be easily tuned for particular applications by a careful selection of a wide variety of cations and anions. A NIST database of ILs is available, where various physicochemical properties of different ILs are documented. ILs have been employed in various applications in areas such as electrochemistry, separation techniques, and catalysis.[16,18–21]

The most common cations in ILs include imidazolium, pyridinium, pyrrolidinium, tetraalkyl ammonium, phosphonium, and sulfonium. Furthermore, there are a wide variety of anions that can be used to accompany the cation, but the most common are tosylate, ($C_7H_7O_3S^-$), tetrafluoroborate (BF_4^-), hexafluorophosphate (PF_6^-), bis(trifluoromethylsulfonyl)imide (NTf_2^-), and dicyanamide ($N(CN)_2^-$). These cations and

anions can form stable, room-temperature ionic liquids with varying properties.[22,23] For example, the [C_4mim][PF_6] IL is stable at room temperature, possesses poor water solubility and high density (denser than water, but less dense than chloroform), and thus has found application in liquid-liquid extraction methods.[24] Ultimately, the physicochemical properties of ILs are dependent on the properties of the cation and anion from which they are composed.

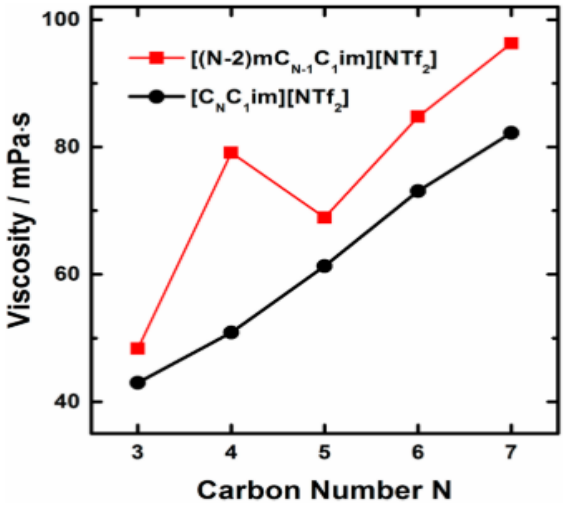

Figure 4: Viscosity of linear ILs (black line) as a function of their alkyl chain length compared to their branched counterparts (red line) with the same carbon chain length. Reproduced from ref. 10 with permission.

Thus, much research has been dedicated toward understanding IL behaviour not only in regard to the cation and anion size, but also their shape, symmetry, alkyl chain length and many other factors. For example, Quitevis *et al*. reported on how alkyl chain branching affects the physicochemical properties of imidazolium-based ILs (Figure 4).[10] It was found that the branched ILs experienced higher glass transition temperatures, viscosities, and melting temperatures compared to their linear counterparts. An explanation for this may lie in liquid phase packing. Maginn *et al.* reported that branched ILs showed more stable packing between the cation and anion in the liquid phase compared to their linear counterparts.[25] Based on simulations, the branched ILs showed longer ion-pair lifetimes compared to their linear counterparts, which was correlated to higher viscosities of the former. Thus, high viscosities might arise due to the specific arrangement of the ion-pairs so that the anion is blocked from approaching the cation (in this case imidazolium) ring.[25] The effect of aromatic and aliphatic substituents on the thermophysical properties of imidazolium-based ILs has also been investigated by Quitevis *et al*.[22] It was found that aromatic substituents showed

higher T_g and density values compared to their aliphatic counterparts. Higher density values of the aromatic substituents were correlated to higher *C/H* (carbon-to-hydrogen) values and higher T_g values were attributed to their lower decomposition temperatures*l*.[26] Schubert *et al.* found that the T_g of (BF_4^-)-containing aromatic ILs was the highest compared to all other tested ILs, while also having the lowest decomposition temperature. Thus, these results lead to the conclusion that aromatic ILs are generally more stable and possess higher T_g values compared to their aliphatic analogues.

Generally, there are two main steps to the synthesis of ILs. Firstly, the desired cation is synthesised. For nitrogen-based cations, this can be achieved *via* the protonation of an amine by an acid or its quaternization with a haloalkane under raised temperatures.[18] Quaternisation reactions generally yield salts consisting of a desired cation and a halide. An example is the reaction between 1-methylimidazole and 1-chlorobutane at reflux (70°C), resulting in the formation of [C_4mim][Cl].[24] However, in order to tune the properties of the resulting salt, anion exchange is undertaken, which yields the desired cation-anion pair. For example, Dinares *et al.* reported on the preparation of various imidazolium-based ILs with varying anions using an anion exchange resin.[27] Figure 5 shows the range of anions tested to perform the halide anion exchange. Successful exchange of the bromide or iodine anions with anions shown in Figure 5 was achieved. This also showcases why ILs are called "designer" solvents – the capability to exchange anions relatively easily to form ILs with different anions, and consequentially, different properties.

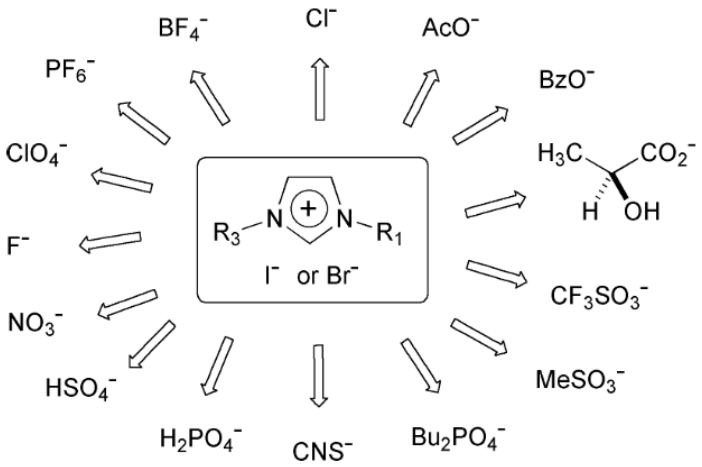

Figure 5: Anions selected to perform halide exchange *via* the anion exchange resin method to form imidazolium-based ILs. Reproduced from ref. 27 with permission.

ILs are generally characterised by thermogravimetric analysis (TGA) and differential scanning calorimetry (DSC), which provide information about thermal properties such as melting point, thermal stability, glass transition temperature and degradation temperature.[28,23] A DSC trace of 1-octyl-3-methylimidazolium hexafluorophosphate, [C_8mim][PF_6], is shown in Figure 6. The glass transition of [C_8mim][PF_6] is approximately at -75°C along with an exothermic peak between -25°C and 0°C, indicating the reorganisation of water molecules prior to melting as postulated by the authors. The presence of water molecules is of no surprise as ILs are generally hygroscopic. In order to minimise the water content, ILs can be pre-treated before use in a standard or vacuum oven or a rotary evaporator, then stored in a tightly sealed vial, desiccator or under argon atmosphere.[22,24,29] Infrared (IR) spectroscopy can be used to determine the presence of the desired functional groups in various ILs. As discussed, anion exchange can be used to introduce a wide variety of anions with different functionalities, and IR spectroscopy can be utilised to determine the presence of such anions. ^{1}H and ^{13}C NMR are generally used to assess the purity of ILs.[30] However, due to the viscous nature of many ILs, high resolution spectra can be difficult to acquire. This is because increased viscosity results in shorter relaxation times, leading to broader spectra which are difficult to resolve. Instruments such as titrometers, coulometers, viscometers, and densimeters are very useful for measuring the physicochemical properties such as density, viscosity and surface tension.

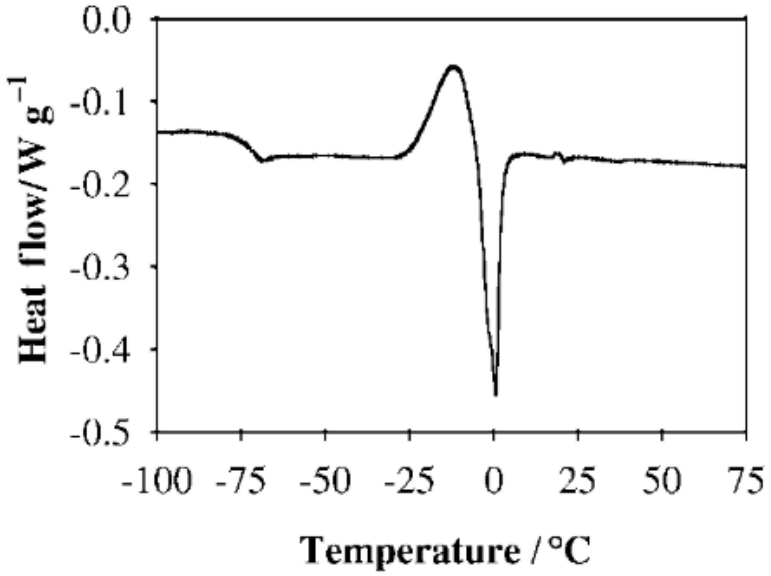

Figure 6: DSC trace of [C_8mim][PF_6], with a glass transition at approximately -75°C (exothermic up). Reproduced from ref. 23 with permission.

1.1.1 Room-Temperature Ionic Liquids

Room-temperature ionic liquids (RTILs) are currently one of the most desirable types of IL for use as solvents. RTILs are easy to use and do not require elevated temperatures to reach their liquid phase. Understandably, a significant amount of research has been put into understanding and characterising these ILs as the scientific community is searching for alternatives to replace traditional organic solvents that are harmful to human health and the environment. It has been found for alkylimidazolium ILs that the longer the alkyl chain on the cation, the higher the melting temperature (T_m) of the IL. This trend is due to inter-chain hydrophobic packing effects for ILs with $n > 8$ (where n designates number of carbon atoms in the alkyl chain).[23] However, for ILs with $n < 8$, T_m does not necessarily increase with the increasing number of alkyl chain. It has been reported that T_m of alkylimidazolium ILs such as [C$_n$mim][NTf$_2$], [C$_n$mim][PF$_6$], and [C$_n$mim[Br] does not increase as the alkyl chain on the cation is increased.[31]It has been shown that in the case of non-spherical ion pairs (with the cation being [C$_6$mim]), the T_m is driven by anisotropic interactions.[32] Ngo *et al.* concluded that the melting point of bulkier asymmetrical cations and anions was lower than that of smaller and symmetrical ones.[28]

The main advantage of RTILs is that they are liquid at room temperature. This has opened up the door for RTILs to be used in various relevant industrial applications. Green chemistry has become a prominent research field over the last few decades, thus prompting researchers to find various applications for RTILs in the field. Recently, a novel family of *closo*-boron-cluster based RTILs for energy storage devices was synthesised by Mohtadi *et al*.[20] The *closo*-boron-based RTILs displayed excellent physical and thermal properties, such as low melting point and high thermal stability, along with compatibility with both lithium and magnesium metals. Remarkably, the *closo*-monocarborane based RTILs exhibit high anodic stability with the magnesium metal, showing the potential of ILs to be tailored compatible with more metals. Although, it must be added that the practical applicability of polyhedral borane hydrides clusters is difficult to achieve due to their generally unstable nature, volatility, and difficult synthesis.[33,34] RTILs have also been successfully used for surface modification of zeolites membranes for CO_2/CH_4 separation.[35] The resulting membranes experience a 44% decrease in CO_2 permeability and a 7-fold increase in CO_2/CH_4

selectivity. These results highlight the potential of RTILs to be used in various applications in the field of green chemistry.

Furthermore, RTILs have found extensive use in electrochemistry. For example, Knipping *et al.* studied the efficiency of various RTILs as lithium-oxygen battery electrolytes.[36] It was found that RTILs offered many advantages of organic liquids at room and elevated temperatures. The main disadvantage of the tested RTILs was the degradation of the imidazolium cation, which lead to low cyclability. However, high thermal stability allows RTILs to be used at elevated temperatures, where their ionic conductivity is higher, thus leading to better performances compared to organic solvents. RTILs can also be employed as nanocomposites for efficient microbial fuel cells (MFCs).[37] In this work, $[C_4mim][BF_4]$ was used to prepare the anode for the microbial fuel cell, which resulted in a highly efficient MFC. In addition to these versatile applications of RTILs, they have also found use in the wood industry for cellulose dissolution and in organic synthesis for catalysis and hydrosilylation.[38]

1.1.2 Imidazolium-Based Ionic Liquids

Imidazolium-based ILs (im-ILs) are one of the most widely studied type of ILs due to their good stability at ambient temperature. In 2001, Huddleston *et al.* reported on the characterization of a set of im-RTILs.[23] It was concluded that the characteristics of the anion are of the utmost importance when it comes to the physical properties of the synthesized ILs. In addition, the authors found that cation substitution is important in regard to water content and hydrophilicity. In a similar study, it was reported that as the alkyl chain length of the imidazolium cation increases, the density of the ILs decreases.[39] For example, the density of $[C_2mim][NTf_2]$ is higher than that of $[C_4mim][NTf_2]$. It is not only the alkyl chain length of the cation, though, that affects the density of a particular IL (Figure 7). As the molecular weight of the anion increases, the density of the resulting IL is higher. Thus, selection of the chemical structure of the cation and anion can have a significant impact on the behaviour and efficiency of the IL in a desired application.

In practical terms, viscosity is one of the most important properties of an IL as it plays a more direct role in scale-up and commercialisation. Im-ILs also hinder the efficiency of fuel cells as their high viscosity inhibits the redox couple diffusion.[40] Im-ILs are known for their high viscosities, which has unfortunately made it difficult to reach their full potential.

Having said this, much progress has been made in order to reduce the viscosity of im-ILs. For example, it has been established that ILs containing the (NTF_2^-) anion have lower viscosities compared to ILs containing the nonfluorinated anion analogue.[41] In addition, im-ILs with mid-range (3-6 carbon atoms) alkyl chain lengths also experience lower viscosities due to decreased van der Waals forces between the imidazolium cations and increased electrostatic interactions between the cation and the anion.[42] These results indicate that there is much potential to engineer low viscosity im-ILs for smoother scale-up and commercialisation.

Im-ILs have also been widely studied and applied as solvents.[43,44] The need for environmentally benign solvents is vastly increasing due to the toxic nature of traditional organic solvents, most of which are classified as volatile organic compounds (VOCs). This has driven research toward next-generation solvents such as im-ILs. The main advantages of im-ILs over traditional solvents is that the former do not emit such a large quantity of VOCs to the atmosphere due to their non-volatile nature. Kumar *et al.* recently reported on the use of im-ILs for the dissolution of lignin from water hyacinth.[44] The authors reported that both hydrophobic and hydrophilic interactions between the solvent and lignin were responsible for efficient dissolution. However, longer alkyl chain im-ILs were not as efficient as shorter chain im-ILs, possibly due to steric hindrance.

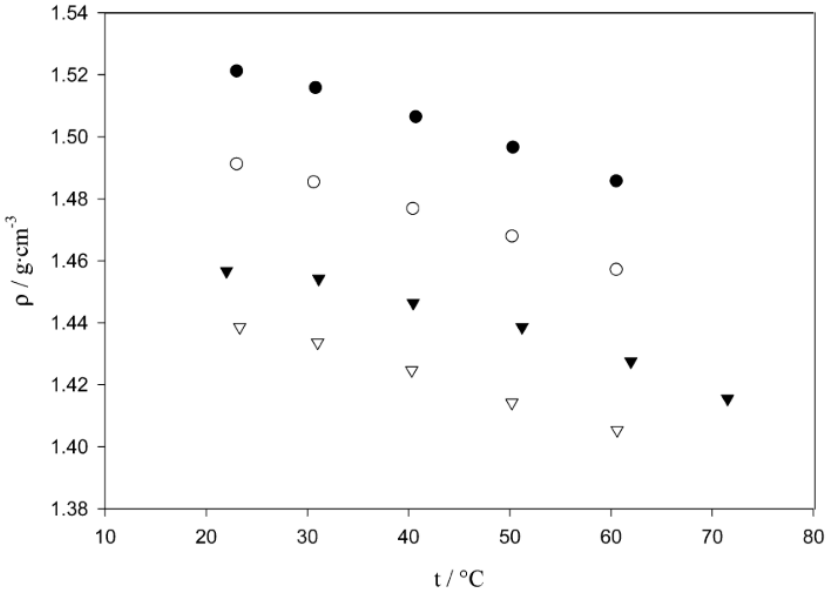

Figure 7: Density of a set of ILs with varying chain lengths bearing the same anion, [NTf_2]. Cations: Black circle – [C_2mim], white circle – [C_2C_1mim], black triangle – [C_3C_1mim], white triangle – [C_4mim] Reproduced from ref. 38 with permission.

1.1.3 Phosphonium-Based Ionic Liquids

Phosphonium-based ILs (P-ILs) are another type of ILs that have gained much attention in recent decades. The research into P-ILs picked up in the late 1990s and early 2000s when multiple reports described their application in various synthetic reactions, such as hydroformylation, Heck reactions, and Suzuki cross-coupling reactions, where they are used as novel solvents.[45–47] Since then, their application has widely expanded into fields such as chromatography, supercapacitors, and antifouling.[48–50] The interest in P-ILs has rapidly grown since and has been sustained for a decade. More recently, they have been utilised in applications such as wastewater purification, CO_2 capture, and biodiesel production.[9,51,52] The ongoing popularity of P-ILs is likely to result in their utilisation in many more applications. P-ILs are relatively new solvents compared to im-ILs and as a result are relatively underexplored. Research into P-ILs is likely to increase as they possess properties that im-ILs do not, such as incapability of aromatic interactions and less efficient hydrogen bonding.

These unique properties are potentially beneficial as they can prevent P-ILs from interacting with desired compounds. For example, the lack of hydrogen bonding capabilities results in a hydrophobic behaviour of P-ILs, which can be used for extraction purposes in polar media. For example, two P-ILs were used for the efficient extraction of phenolic compounds from water.[9] The results showed that the tetraalkylphosphonium-based IL extracted more than 99% of 2,4-dichlorophenol at a volume ratio of 1:135 P-IL:water. A commercially available P-IL was also used for the extraction of zinc from a multi element mixture under acidic conditions with 99% purity.[53] These results demonstrate how the unique properties of P-ILs can be used for efficient extraction applications.

The nomenclature of P-ILs is similar to that of im-ILs with no changes to the anions, but with slight changes toward the cation nomenclature. Namely, the cation is designated as P for phosphonium, to which numbers in subscript are added indicating the length and number of alkyl chains. For example, the trihexyltetradecylphosphonium cation with four alkyl chains is designated as $(P_{6,6,6,14})^+$. So, nomenclature of the IL trihexyltetradecylphosphonium bis(trifluoromethylsulfonyl)amide is $[P_{6,6,6,14}][NTf_2]$.

In terms of their synthesis, the main two routes for the preparation of P-ILs are quaternization and metathesis.[54] For example, an S_N2 reaction between a tertiary phosphine

(PR_3) and a haloalkane (R'X) can be used to prepare asymmetrical tetraalkylphosphonium ionic liquids $[PR_3R'][X]$. An advantage of such reactions is their superior kinetics compared to similar reactions with amines. This is due to the larger radii and polarizability of tertiary phosphines. Overall, they are synthesised in a similar manner as other ILs.

The thermal properties of P-ILs have been studied extensively. Their thermal stability is mainly controlled by the cation or by the strength of the cation-anion interactions.[55] P-ILs generally exhibit high thermal stabilities – above 300°C and sometimes even above 400°C.[56] In addition, they possess higher thermal stability in basic and nucleophilic environments compared to im-ILs as they do not have any acidic protons unlike the latter. Thus, P-ILs can be utilised more efficiently than im-ILs in applications that require such conditions (for instance, synthetic chemistry reactions under basic conditions).

Even though the thermal properties seem to be mainly guided by the nature of the cation, the anion has a more significant effect on density. Bhattacharjee *et al.* noted that P-ILs containing anions with higher molecular weights have higher densities.[57] This behaviour seems to be common in ILs in general as the density of im-ILs is also governed by the molecular weight of the anion. Increasing the alkyl chain length of the cation substituents results in a lower density of the P-IL due to the low density of methylene groups.

The viscosity of P-ILs is governed by π-π interactions, which can be introduced with various anions. For example, the viscosity of $[P_{i(444)1}][Tos]$ is greater than that of P-ILs like $[P_{4441}][CH_3SO_4]$, $[P_{8888}][Br]$ and $[P_{4442}][(C_2H_5O)_2PO_2]$, which do not participate in π-π interactions.[57] Similar trends have been observed for ILs containing imidazolium and pyridinium cations.[22] However, viscosity data is apparently difficult to acquire accurately since large variations of up to 167% occur for the same material in different data sets. This is most likely due to the handling difficulties associated with ILs as they are very sensitive to atmospheric moisture.

1.1.4 Toxicity of Ionic Liquids

The excitement around the research of ILs has been mostly due to them being believed to be environmentally benign. For example, their non-volatile nature significantly decreases their waste management costs. Furthermore, due to their designer properties, ILs can be tailored to increase the yield of a reaction when used as a solvent while also limiting the waste.[58]

However, even though ILs have been generally considered to be “green” solvents, they can exhibit significant toxicity. The belief of ILs being a “green” solvent has been put under high doubt.[59,60] For instance, many ILs are corrosive due to the presence of halogen atoms, which can dangerously react with water. Furthermore, it has been suggested that ILs can have more toxic effects on aquatic life compared to organic solvents based on research demonstrating significant DNA damage in zebrafish.[60] The olive tail moment (OTM), which indicates the distance of the head (genetic material nucleus) and the tail (resulting “tail” after DNA damage), was used to quantify the DNA damage caused by the ILs (Figure 8). Simply put, the larger the distance between the head and the tail, the more significant the damage. This means that if the use of environmentally harmful but efficient ILs increases to the industrial scale, they can have a very damaging impact on aquatic life. Obviously, this outcome must be avoided. Thus, research into the remediation of IL toxicity will play a vital role in their large-scale use.

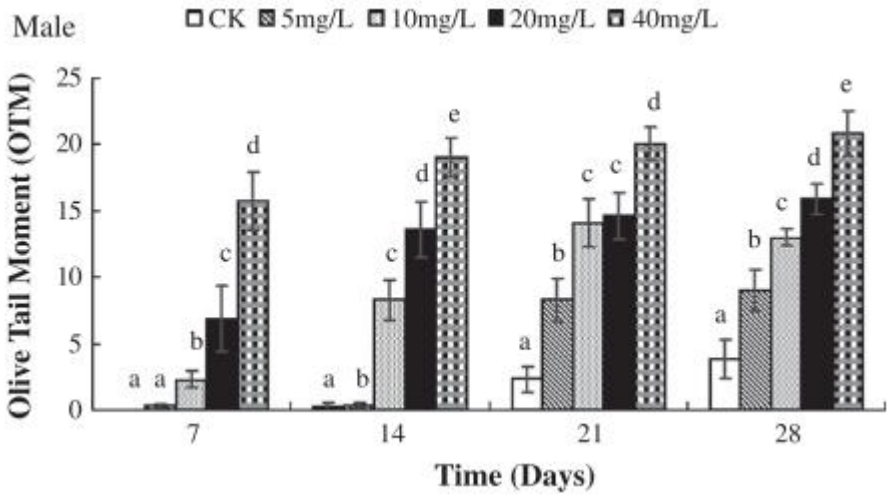

Figure 8: Olive tail moment of male zebrafish after exposure to various concentrations of [C_{10}mim][Br]. Reproduced from ref. 60 with permission.

Furthermore, ILs can have a negative impact on the environment due to their low biodegradability. Oliveira *et al.* tested four protic ILs for their biodegradability *via* the chemical and biochemical oxygen demand methods (COD and BOD).[61] After 48h of incubation, the percent of consumed oxygen before and after incubation is measured to determine the biodegradability of a compound. COD describes a chemical’s capability of oxidising organic matter in liquid media (units of mg O_2 L^{-1}). BOD describes how much oxygen is consumed during the biodegradation process of the organic matter, expressed in

the same units as COD. Numerically speaking, if the COD test values are at least twice as high as the BOD values, it can be assumed that the material is non-biodegradable. All tested ILs exhibited BOD/COD ratios of below 0.03. These results clearly illustrate the non-biodegradability of some protic ILs. Many other reports have highlighted the non-biodegradability and negative environmental impact of some ILs.[62,63] In fact, it has been recently concluded that most ILs should not be considered environmentally safe chemicals.[63]

In order to synthesise biocompatible ILs, their cytotoxicity must be well understood. Sarkar *et al*. reported on the cytotoxicity of im-ILs toward the model oleate ethyl amine membrane.[64] When the pH of the environment around fatty acids is similar to that of their pK_a, they spontaneously form bilayer vesicles. These vesicles can be treated as model membrane systems to evaluate the cytotoxicity of a chemical based on the extent of their swelling in the presence of a toxic chemical. Swelling is the result of the insertion of the IL into the bilayer vesicle. The authors concluded that the imidazolium cation caused swelling of the vesicle via strong electrostatic and hydrophobic interactions through its long alkyl chain. In another study, a variety of ILs was tested for their cytotoxicity.[65] The cytotoxicity was found to be dependent on time; long alkyl chain phosphonium ILs showed cytotoxicity within 2 hours while it took other ILs longer. There seems to be a general trend that longer alkyl chain ILs are more toxic compared to their shorter chain counterparts. Although, the mechanistic understanding of IL toxicity has not yet been fully unravelled.

Having said this, it is important not to conclude that all ILs have a negative impact on the environment. The purpose of this section was to stress that although ILs possess many favourable properties, it is important to keep in mind the impact some ILs can have on the environment. Promising research into the preparation of biodegradable ILs has been conducted and it seems like the use of "green" ILs is becoming more important than before.[66]

1.1.5 Deep Eutectic Solvents

A new class of ILs called deep eutectic solvents (DESs) are a rising alternative for traditional ILs due to their much greener and less harmful nature. DESs can be prepared *via* the addition of a hydrogen bond donor (HBD) to a hydrogen bond acceptor (HBA) in a stoichiometric ratio. Typical HBAs include quaternary ammonium salts such as choline chloride and acetylcholine chloride, which are generally coupled with common HBDs, such as ethylene glycol, levulinic acid and urea. DESs are widely known for their eutectic points when

compared to the melting point of their constituting compounds. This phenomenon is ascribed to the charge delocalization that results from the interactions between the HBD and HBA, which is also considered to be the main driving force for DES formation.[67,68]

The main advantage of DESs over ILs is their cost-effective environmentally benign synthesis. By simply mixing together hydrogen bond accepting and hydrogen bond donating compounds, the synthesis of the resulting DES proceeds with 100% atom economy. However, such synthesis usually requires elevated temperatures.[69,70] The properties of DESs can be tailored by the careful and rational selection of the HBD to accompany the HBA. Notably, a wide variety of HBDs are commercially available, making a wide variety of DESs possible to synthesise. For instance, choline chloride (ChCl) is known for its non-toxicity and biodegradability. A 2:1 mixture of urea:ChCl (ChU) stirred at 80ºC yields a homogeneous liquid. Even though it is not fully understood how DESs form, a model for ChU formation was proposed based on spatial density functions.[67] In this, two urea molecules are hydrogen bonded to a chloride with a bond distance of 2.2 Å while choline forming hydrogen bonding interactions with the chloride as well. These interactions result in the sandwich-type structure of the ChU DES (Figure 9).

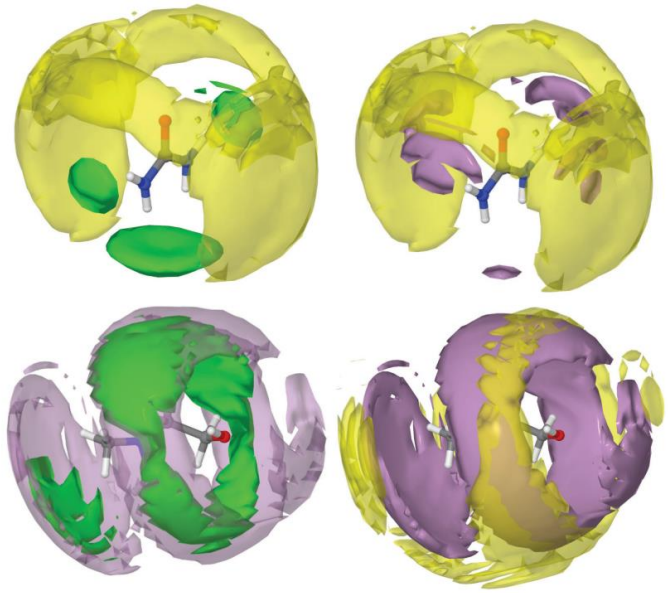

Figure 9: A proposed three-dimensional structure of the DES reline. Yellow – choline cations, purple – urea molecules, green – chloride anions. Reproduced from ref. 67 with permission. Published by the Royal Society of Chemistry.

Practically speaking, DESs possess advantages over ILs not only due to their facile synthesis, but also in terms of biodegradability. The biodegradability of ChCl also applies to one of its derivatives, acetylcholine chloride (AChCl), which is present in the human body and also enhances the ion permeability of plant roots.[17] Thus, the lifecycle of certain DES is not only cost-effective but also environmentally friendly and sustainable. For these reasons, DESs have been widely applied in various fields, such as electrochemistry[71], extraction processes[70,72] and gas absorption[73], in addition to being widely used as solvents for different synthetic strategies.[74,75]

1.2 Porous Materials

Porous materials have been widely used for their unique properties for a variety of applications such as ion exchange, adsorption, separation, and catalysis.[76–79] The most well-known porous substances are zeolites, which are a family of aluminosilicates that naturally occur in crystalline hydrate form. In addition to zeolites, other porous substances such as porous metal-organic frameworks (MOFs), aerogels, polymers, and nanomaterials have recently been developed.[80–83] In such cases, porosity can be used in various ways. For example, He *et al*. reported a MOF catalyst for chemical fixation of carbon dioxide, where the pores of the MOF material act as sites to facilitate the conversion of carbon dioxide to carbonic ester product with high yields.[82] In another example, molybdenum phosphite (MoP) nanowires were used for hydrogen evolution reaction (HER), where the porosity of the nanowires was responsible for the excellent efficiency of HER in various pH conditions.[84] The authors stated that the porosity of the nanowires was responsible for an increase in the number of active sites, which played a significant role in the efficiency of HER.

Porous materials can be classified by their pore size – ultramicropores are classified as pores with diameters up to 0.7nm, micropores and mesopores range from 0.7 to 2nm and 2 to 50nm, respectively, and pores larger than 50nm in diameter are macropores. Furthermore, knowing the pore size, diameter and structure is of utmost importance for their function in a chosen application. For example, in the use of cellulose acetate polymer as an adsorbent material for the uptake of various pollutants, understanding the pore size and distribution of the polymer will give a good indication on what molecules will be able to diffuse through the pores freely and which molecules might be too large to enter.

1.2.1 Techniques for the Characterisation of Pore Properties

One of the most widely used technique for pore size determination in solids is gas sorption.[85,86] This technique allows for a precise measurement of the amount of gas adsorbed on the surface of the porous material, which reveals the pore properties and structure. Furthermore, this technique is relatively fast and can be used with various gases such as Ar, CO_2, and N_2 at low temperatures. In addition, the use of methane gas in the gas adsorption technique has also been reported.[87] The gas sorption method allows for the calculation of the specific surface area of a porous material. For example, the efficiency of hydrogen storage applications is of utmost importance upon its use as an alternative fuel. One of the most promising methods for hydrogen storage is its adsorption by porous materials. Rapid adsorption and desorption kinetics and minimal energy requirements associated with the process are the main advantages of the method. The use of N_2 adsorption/desorption isotherm has been described for the hydrogen storage capabilities of nitrogen-doped activated carbon (Figure 10).[1] The authors found that materials composed of ultramicropores and wider pores had a negligible contribution to the uptake of N_2. Thus, gas sorption was effectively used to assess the structural components of the pores, which allowed for the understanding of how the activation temperature affected the pores, which then affected the hydrogen storage efficiency. Amongst the most widely utilised methods to evaluate gas sorption data are the Brunauer-Emmett-Teller (BET) theory, Barrett-Joyner-Halenda (BJH) and various density functional theory (DFT) models.[88,89]

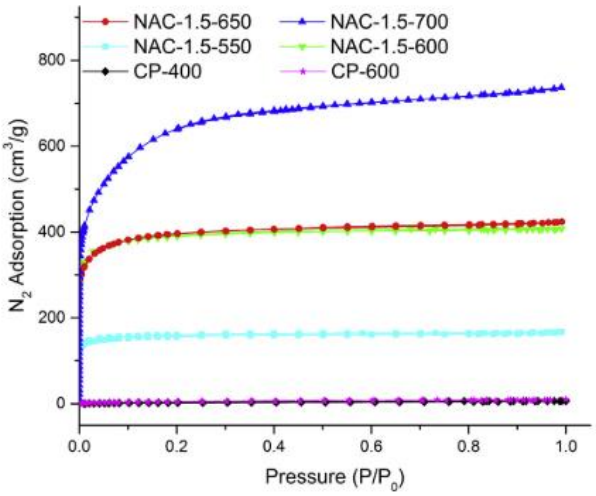

Figure 10: N_2 adsorption/desorption isotherms obtained for the nitrogen-doped activated and non-activated carbons. NAC stands for nitrogen-doped activated carbon and CP stands for carbon precursor. Reproduced from ref. 1 with permission.

In addition to gas adsorption, small-angle and ultra-small-angle neutron scattering (SANS and USANS) have been utilised as indirect methods toward characterising pore structure.[86,90] SANS and USANS both give information about the surface of the porous material, where the scattering occurs. Structural information such as accessible porosity and pore size distribution can be obtained by analysing the scattering intensity. A significant advantage of this method is its non-destructive nature. Compared to small-angle X-ray scattering (SAXS) technique which can be destructive toward radiation-sensitive samples, SANS, by using neutrons instead of X-rays, can see this issue remediated.

Additionally, scanning electron microscopy (SEM) and transmission electron microscopy (TEM) have been used to probe pore properties. These techniques are used to visualise matter on a very small scale. Both utilize the electrons bouncing back from a sample to give an image of its surface. In regard to porous materials, SEM and TEM can be used to visualize and describe a porous structure based on its surface. For example, Zhang *et al.* described the use of SEM and TEM to reveal the porous nature of a magnetic porous carbon.[91] Ultimately, both SEM and TEM are not quantitative methods and are used to confirm or reveal the porous nature of a material.[92,93,94]

1.3 Porous Liquids

So far, only solid porous materials have been discussed. Even though they can achieve high efficiencies for particular tasks, applications involving separation and absorption are easier to control with liquids, can achieve higher efficiencies and are more energy-effective.[95] For example, it has been reported that it is easier to achieve the retrofitting of liquid circulation systems for post-combustion capture of carbon dioxide.[8] In addition, liquid materials have been widely implemented into various large-scale applications, such as carbon capture via amine-based liquids.[6] Thus, a free-flowing material with permanent porosity can be of high demand in industrial applications.

1.3.1 Type 1 Porous Liquids

Since the introduction of PLs, significant advances have been made in the field. As porous compounds generally have high melting points, the only viable method to prepare Type 1 PLs is *via* elevated temperatures to force the solid-to-liquid transition. However, melting processes can have negative effects on the pore properties of porous compounds, making Type 1 PLs extremely difficult to prepare.[96] Thus, the application of Type 1 PLs as liquid

sorbents is difficult to envisage. Furthermore, examples of Type 1 PLs are limited due to the difficulty in efficiently producing such systems. Nonetheless, Coudert *et al.* reported on the synthesis of the first MOF-based Type 1 PL by melting ZIF-4 MOF at 865K, while retaining intrinsic porosity.[97] Another Type 1 PL was reported by Dai *et al.* based on hollow silica (HS) spheres.[98] HS spheres were treated with organosilane and poly(ethylene glycol) (PEG) tailed sulfonate canopy to yield a clear liquid. The porosity of the resulting hollow sphere was confirmed *via* N_2 adsorption/desorption and TGA. This approach seems to be more promising of the two examples due to the ability to modify the functional groups of the canopy, which can aid in controlling the diffusivity of gas particles through the PL. Most notably, a recyclable Type 1 PL was prepared by functionalising an aniline-based precursor with PEG-imidazolium to yield neat liquid cages with empty cavities.[99] Long PEG chains were used to decrease the melting point of the resulting cage below room temperature resulting in a viscous liquid. In addition, the imidazolium cation prevented the chains of the cage from interpenetrating the positively charged cavities. This porous liquid was employed for the uptake of environmentally dangerous chlorofluorocarbons.

1.3.2 Type 2 Porous Liquids

Type 2 PLs have been more widely reported compared to Type 1. The first Type 2 PL was demonstrated by Cram *et al.* in 1994.[100] The authors demonstrated that by heating a hemicarcerand in diphenyl ether solution to 195°C, the guest *N*,*N*-dimethylacetamide molecule was removed from the void of the carcerand host. Thus, empty hemicarcerand molecules remained in the solvent, classifying the system as a Type 2 PL. In 2003, Hsu *et al.* demonstrated an inorganic example of a Type 2 PL.[101] An ionophilic molecular box, Co_4Ru_4 (Figure 11), was dissolved in acetonitrile while retaining its empty voids and rigidity. The box was capable of encapsulating small ions such as $CH_3NH_3^+$, K^+, and Cs^+ while keeping acetonitrile solvent molecules outside of the pore.

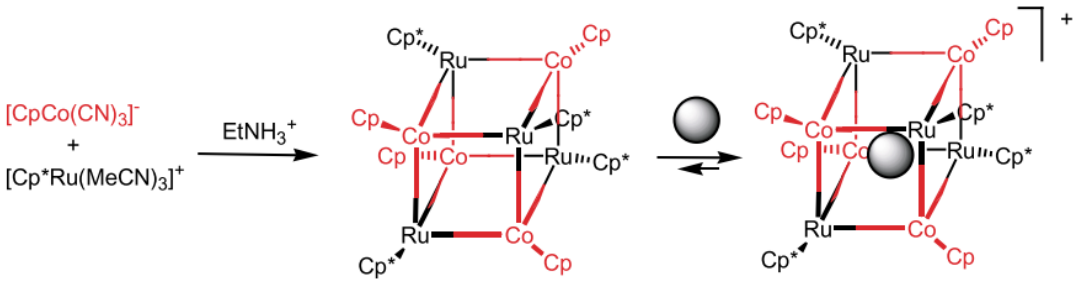

Figure 11: Preparation of the Co_4Ru_4 metallocube with empty and filled void. Reproduced from ref. 100 with permission.

The aforementioned Type 2 PL prepared by James *et al.* is an archetype of the potential of PLs to overtake standard sorbent liquids in their commercial use.[8] However, the main disadvantage of their method is the complexity and cost of the synthetic route combined with the use of ethers, which are known to be environmentally "unfriendly" as groundwater contaminants.[102] Still, this report serves as a strong starting point toward designing more cost-effective and environmentally friendly Type 2 PLs.

1.3.3 Type 3 Porous Liquids

The first Type 3 PL was prepared by Liu *et al.* in 2014.[103] A porous slurry composed of ZIF-8 nanoparticles dissolved in glycol-2-methylimidazole was prepared for selective CO_2 capture. It was found that the presence of 2-methylimidazole significantly increased the solubility of CO_2 in the solvent, enabling it to be efficiently used at low partial pressures. The efficiency of this PL was compared to that of current industrial technology used to separate CO_2 from biogas. Based on column breakthrough tests, it was determined that the CO_2 breakthrough occurred much slower in the ZIF-8 containing PL (Figure 12), showing its superior performance. Most Type 3 PLs prepared so far have utilised the ZIF-8 MOF and share similar approaches. For example, the dispersion of ZIF-8 in various bulky ILs has resulted in the successful preparation of Type 3 PLs.[103–105]

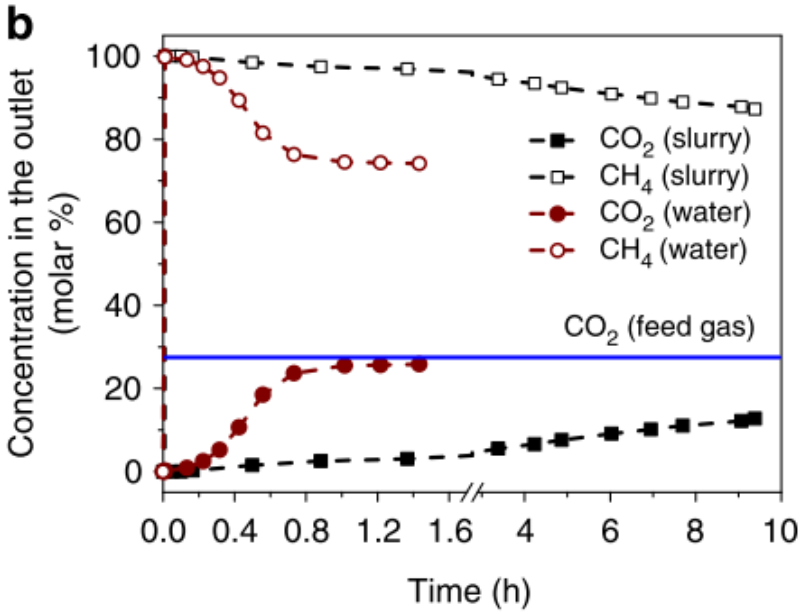

Figure 12: Column breakthrough tests showing the ZIF-8 containing slurry performance compared to industrial water-based technology. Reproduced from ref. 102. This content is licensed under a Creative Commons Attribution 4.0 International License, which can be accessed *via* the following link: https://creativecommons.org/licenses/by/4.0/.

However, more recently, a report describing the preparation of Type 3 PLs using a variety of microporous liquids in combination with non-ionic solvents for the purpose of gas uptake.[106] The range of porous hosts included zeolites, MOFs and a porous organic polymer. The range of solvents included various oils, such as silicone, sesame, sunflower and olive oil. Notably, many dispersions exhibited higher gas uptake compared to their solid counterparts and could potentially be used for gas separation applications.

Overall, it seems like the use of bulky ILs is the standard route to preparing permanently porous systems. It has been shown that liquids with permanent porosity can be prepared upon the careful selection of the solvent and pore generator molecules. This is very promising toward utilising DESs, a type of IL, which are also ionic by nature, but have the advantage of being more cost-effective and "green". In this context, employing environmentally friendly ILs or DESs as the solvent medium for the preparation of PLs can be very promising, as the potential of PLs to become commercially employable is excellent.

1.4 Project Aims

The main objective of this work is to prepare Type 2 and Type 3 porous liquids using involatile solvents such as ILs and DESs. For Type 2 porous liquids, dimeric and hexameric metal-organic nanocapsules (MONCs) prepared by Atwood *et al*. were chosen as the porous hosts.[107–109] Single-crystal structure analysis performed *via* the Cambridge Structural Database suggests that the cavity window sizes of the MONCs are sufficient to allow for the uptake of small volatile organic compounds (VOCs). The pore window sizes were determined by measuring the distance between two sets of closest adjacent hydrogen atoms. For Zn-PgC_3, these are the hydrogen atoms labelled blue and orange on Figure 13e. This estimation of the window sizes (taking into account the van der Waals radius of hydrogen atoms, 1.2 Å[110])lead to the values of 3.171 Å by 3.120 Å (distance between the blue and green hydrogen atoms, respectively). The cavity windows of Mg-PgC_3 and Cu-PgC_3 are 3.032 Å by 3.097 Å and 3.033 Å by 3.054 Å, respectively. For comparison, the cavity window of the cucurbituril CB[5] is approximately 3.0 Å and it has been found that it can only include small molecules such as water, methanol, and acetonitrile.[7] A selection of

various sizes of VOCs are shown in Figures 13a-d. Smaller molecules such as chloroform and dichloromethane are small enough to enter the cavity of each MONC. However, larger molecules such as benzene and toluene are expected to not enter the cavity windows due to steric hindrance.

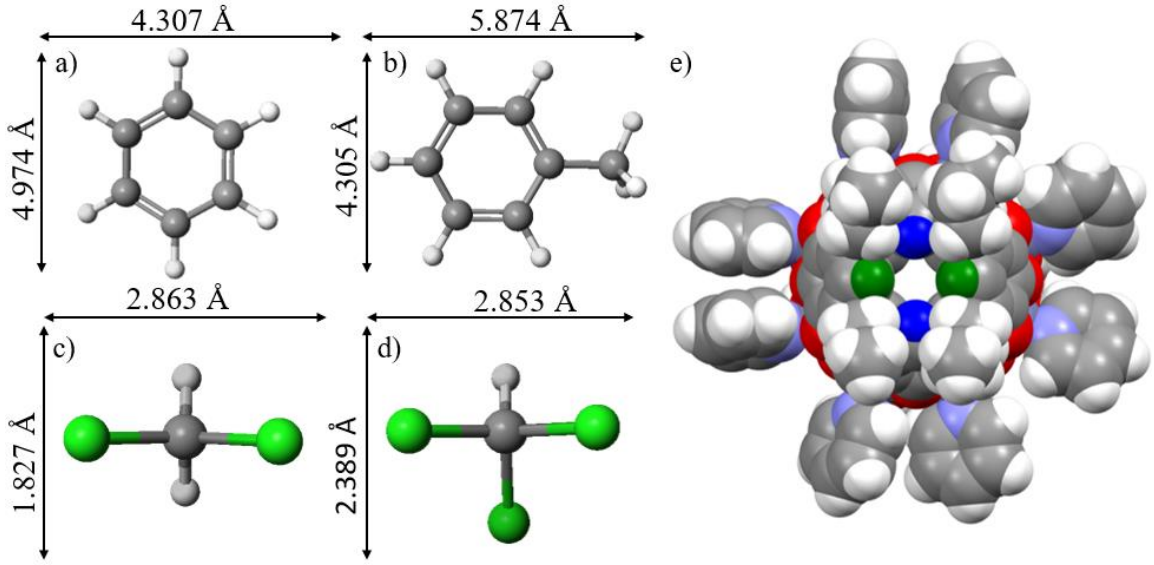

Figure 13: Depiction of Zn-PgC$_3$ and the guest molecules tested: a) benzene, b) toluene, c) dichloromethane and d) chloroform. Distances were calculated after using the MO-G geometry calculation with PM6 parameters using the Scigress software. e) Spacefill view of Zn-PgC$_3$ (referenced as YEVVOL in the CSD database). Grey: C, green: Cl, red: Zn, purple: N, dark green: H, blue: H. The cavity window size of the MONCs was measured between the hydrogen atoms shown as blue and dark green.

For Type 3 porous liquids, Basolite F300 metal-organic framework (MOF) was selected as the porous host. This MOF contains pores of approximately 2 nm in size suggesting that the VOCs depicted in Figure 15 would not be sterically hindered from the pores of these MOFs.

In terms of solvent selection, one of the main constraints is that the solvent molecules must be bulky enough not to occupy the cavities of the MONCs. In this context, ionic liquids are a good choice of solvent as they exist in various shapes and sizes. Solvent screening can be performed efficiently as a wide selection of ILs exists. Three ILs have been selected for the preparation of PLs in this work. More specifically, an imidazolium-based IL ([C$_4$mim][BF$_4$]) and two phosphonium-based ILs ([P$_{6,6,6,14}$][NTf$_2$] and [P$_{6,6,6,14}$][TMP]). These ILs differ in cation and anion hydrophilicity and size. For instance, [C$_4$mim][BF$_4$] is smaller, protic and more hydrophilic compared to the P-ILs. However, the P-ILs only differ

in the nature of the anion to help further investigate and understand their solvation capabilities. The cations of both P-ILs are rather hydrophobic and large, but the anion of $[P_{6,6,6,14}]$[TMP] is more hydrophobic. Overall, the aforementioned ILs will provide a good starting point for the preparation of porous liquids.

2. Results and Discussion

2.1 C-Propylpyrogallol[4]arene

C-propylpyrogallol[4]arene (PgC_3) was prepared through a condensation reaction between butyraldehyde and pyrogallol under acidic conditions. Refluxing this mixture in ethanol for 24 hours gave a dark red precipitate, which was recrystallised from methanol resulting in a white powder in 21% yield. Recrystallisation gave good quality crystals and single crystal X-ray diffraction (SXRD) studies were performed resulting in a precise structure determination with R_1 = 5.56%. The crystal was determined to be a novel PgC_3 hexasolvate (Figure 17, henceforth referred to as PgC_3-MeOH) and was also characterised by ^{1}H NMR spectroscopy, proton decoupled ^{13}C NMR spectroscopy and thermogravimetric analysis (TGA).

Based on its structure (Figure 14a), PgC_3 is fourfold symmetric in solution. The unique portion of the molecule contains four different types of hydrogen atoms on the alkyl substituent, one hydrogen atom of an aromatic CH group, and two different hydroxyl hydrogen atoms. In total, seven ^{1}H NMR signals (excluding solvent resonances) are expected. Peaks at 7.22 and 8.12 ppm were observed in a 1:2 ratio, respectively, which are assigned to the hydroxyl hydrogen atoms. This assignment was confirmed by the addition of a few drops of deuterated water, which resulted in the disappearance of these signals due to H/D exchange. In addition, no unassigned peaks remained. Eight distinct signals were observed in the $\{^1H\}^{13}C$ NMR spectrum, further confirming the successful synthesis of the calixarene. The results of both ^{1}H NMR and $\{^1H\}^{13}C$ proton decoupled NMR spectra were in close agreement with previous results.[111]

Based on the CSD, there are only three known crystal structures of PgC_3 containing methanol (reference codes DOQFAS, LUMXEY and RORBAD).[112–114] However, these crystal structures were obtained as cocrystals using 1-(2-pyridylazo)-2 naphthol, rhodamine B and xanthone as co-formers, respectively. These co-crystals will be referred to as PgC_3-PAN, PgC_3-RB and PgC_3-XAN, respectively. There are many similarities between PgC3-MeOH and the reported crystal structures. For example, all belong to the $P\bar{1}$ space group and exhibit bilayer-type packing. Furthermore, in all crystal structures, PgC_3 is stabilised by inter- and intramolecular hydrogen bonding interactions, suggesting it is an efficient way to crystallise PgC_3 molecules. All structures are in the pinched cone conformation, apart from

PgC_3-RB, which exhibits the conical conformation. The pinched cone conformation exhibits C_{2V} symmetry and has two aromatic rings almost parallel to each other with the other two more flattened (Figure 14b).[115] The conical conformation exhibits C_{4V} symmetry in which all four aromatic rings are angled similarly.

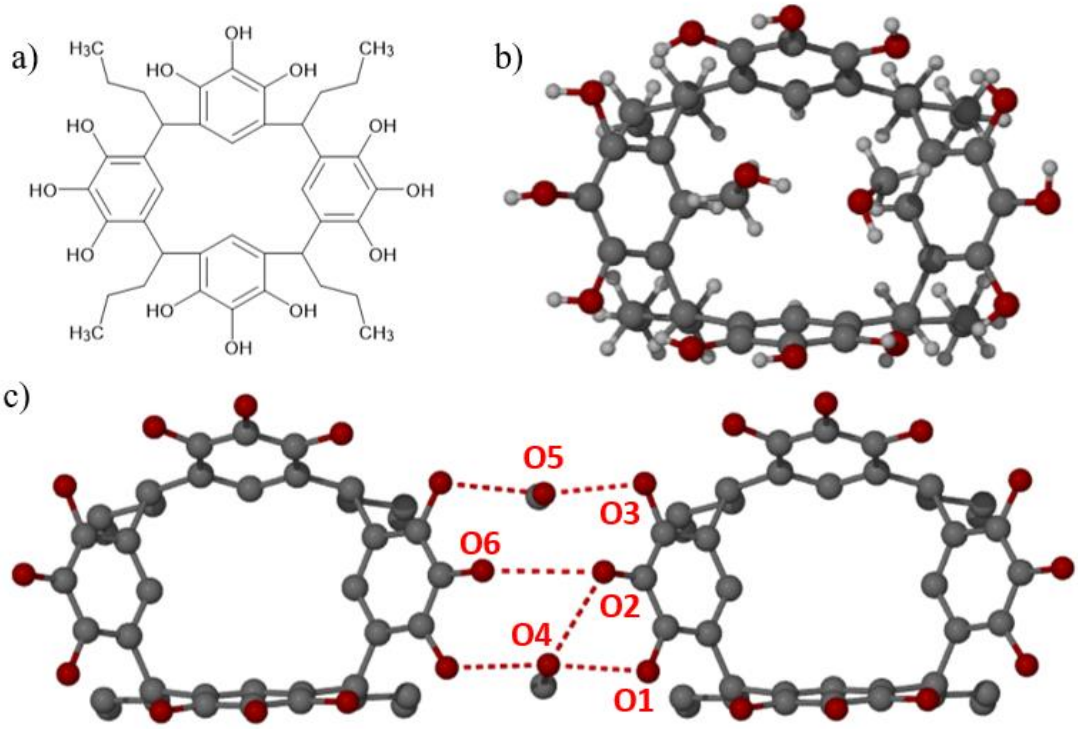

Figure 14: a) Structure of Pg-C_3. b) Top view of the crystal structure of PgC_3-MeOH with two methanol molecules inside the cavity. c) Intermolecular hydrogen bonding between two methanol and PgC_3-MeOH molecules. Hydrogen atoms have been omitted for clarity.

PgC_3-MeOH is triclinic and contains intra- and intermolecular OH···O hydrogen bonding between PgC_3–PgC_3, PgC_3–methanol and methanol–methanol molecules. The intramolecular O···O hydrogen bond lengths between the hydroxyl oxygens of PgC_3 vary from 2.7499(18) to 2.8382(17) Å. Nineteen hydrogen bonds are present in the PgC_3-MeOH structure. Eleven of those are intermolecular hydrogen bonds between methanol and the calixarene. Four are intramolecular calixarene hydrogen bonds and four more are intermolecular methanol-methanol hydrogen bonds.

The intermolecular O···O hydrogen bonding distances vary from 2.5972(19) to 2.939(2) Å. The former value is remarkably short for a neutral hydrogen bond and is more common for ionic hydrogen bonds.[116] In fact, this is the shortest hydrogen bond recorded for

PgC_3. Notably, there are other compounds that exhibit hydrogen bonds this short. For instance, the crystal structure of a cocrystal including *p*-hydroxybenzoic acid (*p*-HBA) and glutaric acid contains a hydrogen bond with the distance of 2.597 Å between the carboxylic acid groups of two adjacent *p*-HBA molecules.[117]

Figure 14c shows intermolecular hydrogen bonding between two PgC_3 and two methanol molecules that are sandwiched between the two calixarenes. Two methanol molecules act as bridging units between the symmetry equivalent PgC_3 molecules *via* five hydrogen bonds. This phenomenon is also observed in the crystal structure of PgC_3-PAN with a slight difference of four hydrogen bonds included in the bridging. The shortest hydrogen bond is between O1 and O4 atoms and arises due to the compression of the two adjacent PgC_3-MeOH molecules by O2 participating in hydrogen bonding with O4. This results in a hydrogen bond between O2 and O6, which has the length 3.0705(18) Å.

The cavity of PgC_3 is occupied by two methanol molecules (Figure 14b). By looking at the packing arrangement, it is revealed that these methanol molecules, among many, are between the hydrophilic ends of separate layers of PgC_3-MeOH molecules and form a hydrogen bonding belt (Figure 15b). Figure 15a displays the bilayer-type packing of the calixarene. This is most likely driven by van der Waals and hydrophobic forces.

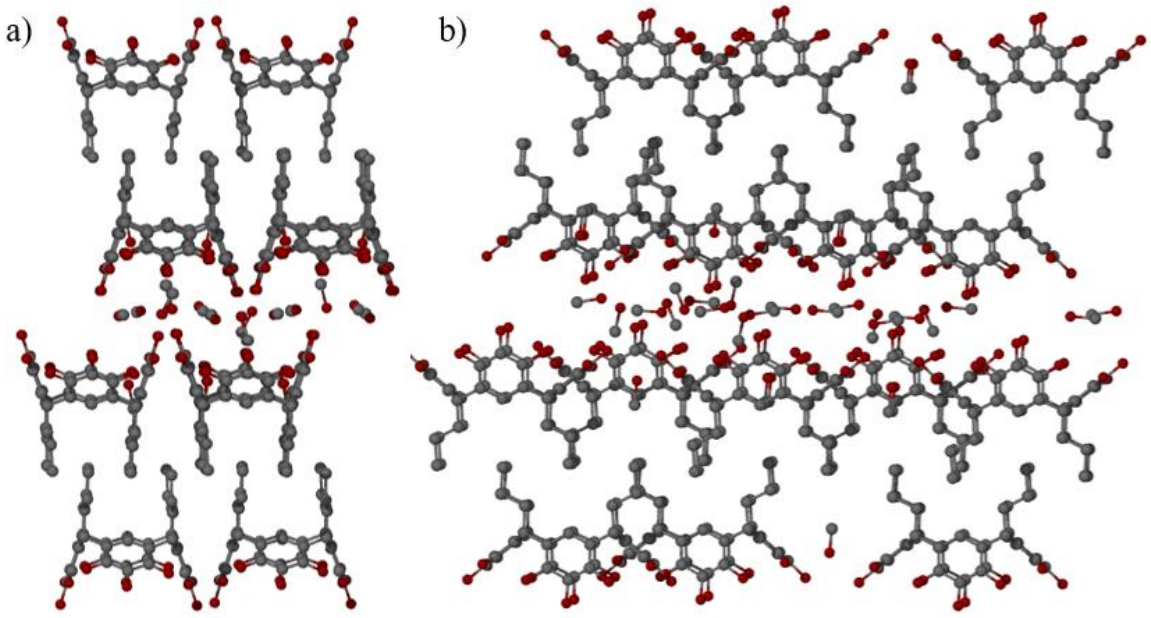

Figure 15: a) Packing arrangement of PgC_3 to illustrate the bilayer-type packing. b) Packing arrangement of PgC_3 as viewed from the side of Figure 15a. Hydrogen atoms have been omitted for clarity.

TGA was undertaken to establish the thermal stability of the as-synthesised PgC_3. It is important to know the thermal stability of this compound as subsequent synthesis requiring elevated temperature will be undertaken (solvothermal synthesis of the magnesium hexamer discussed below). The sample was heated from room temperature to 450°C under helium atmosphere with a ramp rate 10°C min^{-1}. The thermogram revealed a decrease in weight of 1.4% up to 86.9°C, which could be the result of solvent loss from the crystals. A decomposition onset temperature of 360.4°C accompanied by a weight loss of 90% was observed. Hence, PgC_3-MeOH has a high thermal stability and can be used for the synthesis of Mg-PgC_3.

2.2 Magnesium Seamed Hexameric Nanocapsules

Magnesium seamed hexameric nanocapsules (Mg-PgC_3) were prepared *via* a solvothermal method previously reported.[107] A mixture of $Mg(NO_3)\cdot 6H_2O$ and PgC_3 in DMF:MeCN was heated at 100°C overnight, resulting in black prism-shaped crystals. The crystals were characterised by SXRD, NMR spectroscopy, MALDI mass spectroscopy and thermogravimetric analysis.

The crystal structure of Mg-PgC_3 (Figure 16) contains a large amount of disordered solvent molecules and as a result the R_1 value of 14.58% is relatively high. However, the determination is of sufficient precision to give a qualitative picture of the main structure details. The unit cell parameters are very similar to that of the magnesium MONC previously reported and the materials are isomorphous.[107] The Mg-PgC_3 nanocapsules are made up of six PgC_3 ligands and 24 divalent magnesium cations. The coordination bond lengths between magnesium cations and the oxygen atoms of the pyrogallol[4]arene ligand vary between 1.987(7) – 2.068(7) Å. These values are similar to the reported bond lengths, which are between 1.99 – 2.03 Å.[107] Mg-PgC_3 contains eight Mg_3O_3 units in which the Mg–O–Mg bond angles range between 137.2(4) – 140.0(5)° and the O–Mg–O angles are between 99.4(3) – 103.2(4)°. These results are also in close agreement with the reported values. The 24 divalent magnesium cations are in an octahedral geometry. Equatorial positions are coordinated to the O atoms of the PgC_3 ligands and the axial positions are coordinated to solvent molecules. Figure 18b shows the packing arrangement of Mg-PgC_3. The MONCs are stacked in an alternating arrangement, which is most likely guided by the alkyl tails. This type of packing arrangement has also been previously reported for Mg-PgC_3.

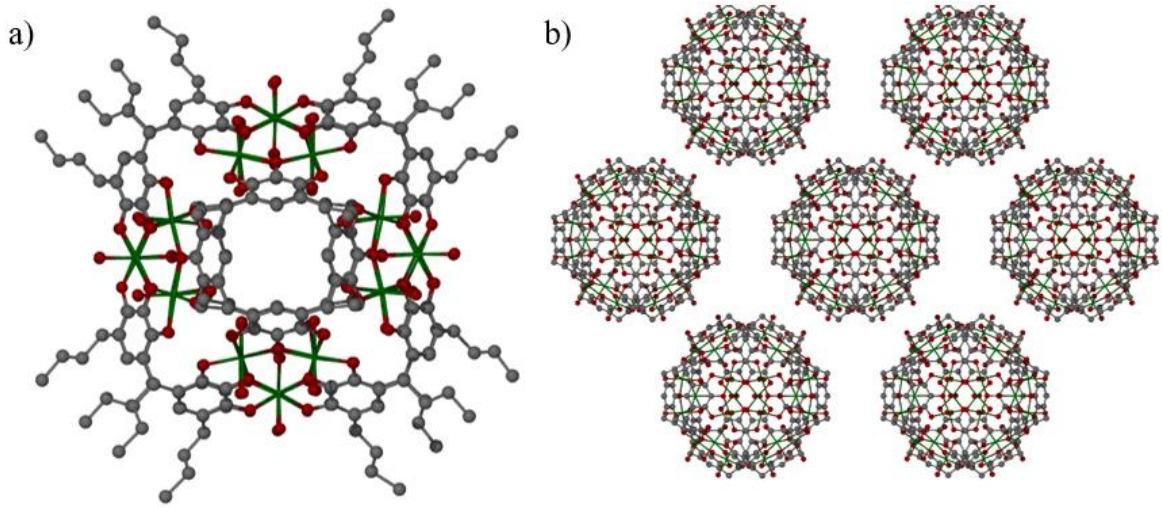

Figure 16: Magnesium seamed metal organic nanocapsules. a) Structure of a single Mg-PgC_3 capsule. Hydrogen atoms have been omitted for clarity. b) Packing arrangement of Mg-PgC_3 viewed down the 001 axis. Hydrogen atoms and alkyl tails have been omitted for clarity.

Performing solvent masking on the disordered solvent molecules inside the Mg-PgC_3 cavity indicated that the volume of the cavity is 782 $Å^3$ and that it contains 505 electrons. It is difficult to accurately determine the contents of the cavity considering it could contain acetonitrile, dimethylformamide and water molecules in any possible combination. Furthermore, it is likely that different combinations of these solvent molecules are inside each Mg-PgC_3 nanocapsule.

MALDI–MS was performed to aid in the characterisation of the contents of the Mg-PgC_3 cavity. Unfortunately, the spectrum contained a wide spread of peaks across the m/z scale which were difficult to assign. This could mean that the as-prepared Mg-PgC_3 crystals are unstable and decompose into various fragments. To support this hypothesis, TGA was performed. The thermogram (Figure 17) revealed that Mg-PgC_3 gradually decomposes and loses 50% of its weight by 148°C. The decomposition pathway most likely lies in the nature of the metal coordination bonds as other MONCs exhibited significantly higher thermal stabilities. The decomposition of these magnesium coordination bonds would lead to various sized fragments as observed in the MALDI-MS spectrum. ^{1}H NMR spectroscopy was also performed on Mg-PgC_3, but no identifiable peaks apart from those of solvent were obtained because of the low solubility of the MONC.

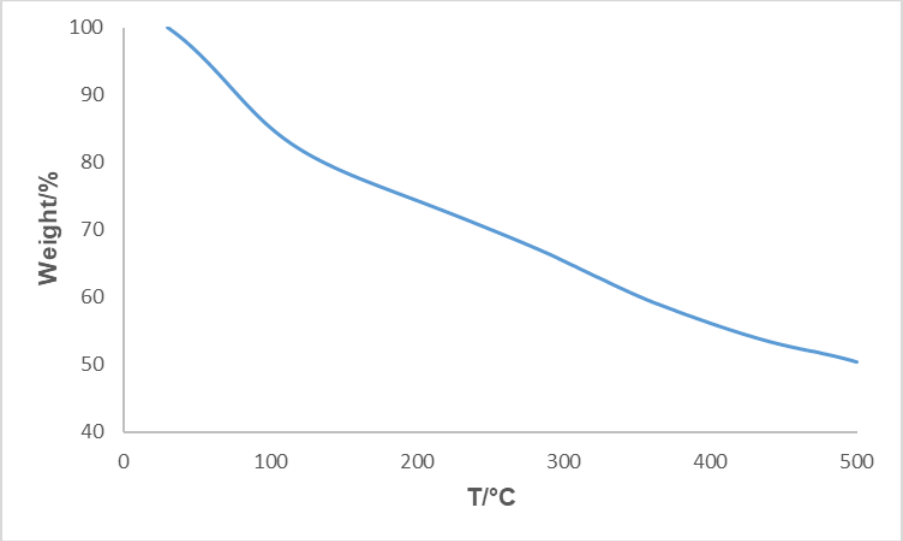

Figure 17: TGA curve of Mg-PgC_3.

Overall, these results show that these magnesium MONCs would be very difficult to implement into porous liquids due to their relatively weak thermal stability. In addition, SXRD analysis showed that these MONCs contain solvent molecules within the cavities, which would be difficult to remove without destroying the Mg-PgC_3 structure. Hence, it was concluded that no further experiments will be undertaken with these MONCs.

2.3 Copper Seamed Hexameric Nanocapsules

Copper seamed hexameric nanocapsules (Cu-PgC_3) were prepared by mixing a methanolic $Cu(NO_3)_2 \cdot 2.5H_2O$ with a methanolic PgC_3 solution. This resulted in a rapid formation of a brown precipitate, which was collected by vacuum filtration. The product was characterised by matrix assisted laser desorption/ionisation (MALDI) mass spectroscopy and TGA. The specific mass of Cu-PgC_3 nanocapsule is 5783.8. Thus, it was expected that peaks at *m/z* values higher than this would appear on the mass spectrum due to the presence of coordinated and trapped solvent molecules.

The (+)MALDI mass spectrum of Cu-PgC_3 has the base peak value of 6409.4. This specific mass corresponds to an ionised fragment of $[M+24H_2O+6CH_3OH+H]^+$ (M = $C_{240}H_{240}Cu_{24}O_{72}$), which suggests that the 24 water molecules could be coordinated to the 24 copper cations, and 6 methanol molecules are most likely trapped inside the nanocapsule cavity. Two more peaks are located at 6443.8 and 6473.6, which correspond to the ionised fragments of $[M+24H_2O+7CH_3OH+H]^+$, *m/z* = 6441.3, and $[M+24H_2O+8CH_3OH+H]^+$, *m/z* = 6473.3, respectively. Similar values were obtained for Cu MONCs with hydroxyl

functionalised PgC_3 alkyl tails, indicating that the desired Cu-PgC_3 has been successfully synthesised.[118] It has been previously suggested that 24 water molecules form a metal-coordinated water cluster inside the capsule cavity.[118] This indicates that the axial copper coordination sites directed toward the inside of the cavity are most likely taken up by these water molecules.

Table 1: MALDI mass fragments of copper seamed hexameric nanocapsules.

m/z found	m/z calc	Fragment	Solvent
6409.4	6409.2	$[Cu_{24}C_{246}H_{313}O_{102}]^+$	$24H_2O + 6CH_3OH$
6443.8	6441.3	$[Cu_{24}C_{247}H_{317}O_{103}]^+$	$24H_2O + 7CH_3OH$
6473.6	6473.3	$[Cu_{24}C_{248}H_{321}O_{104}]^+$	$24H_2O + 8CH_3OH$

The thermal stability of Cu-PgC_3 was evaluated by TGA from room temperature to 500°C under helium atmosphere. The thermogram (Figure 18) shows a similar behaviour to that of PgC_3. A slow decrease of approximately 10% weight is observed up to 250°C, which could indicate the loss of surface and entrapped solvent. The estimated entrapped solvent molecules of the base peak consist of 24 water and 6 methanol molecules (Table 1), corresponding to approximately 10% weight of Cu-PgC_3. This indicates that the cavity window of Cu-PgC_3 is of sufficient size to permit the host-guest exchange of molecules the size of methanol and water. This is followed by a sharp weight loss of approximately 40% with an onset temperature of 338.5°C. The onset decomposition temperature of PgC_3 is 360.4°C, which is very similar to that of Cu-PgC_3. This could indicate that the decomposition pathway starts by the breakdown of the pyrogallol[4]arene ligands rather than the coordination bonds. Nonetheless, these results show superior thermal stability of Cu-PgC_3 over Mg-PgC_3, making it a more desirable MONC for the preparation of porous liquids than the latter. Having said this, it is important to add that the potential application of Cu-PgC_3 as Type 2 PLs was not further investigated due to the time constraints from the ongoing COVID-19 pandemic.

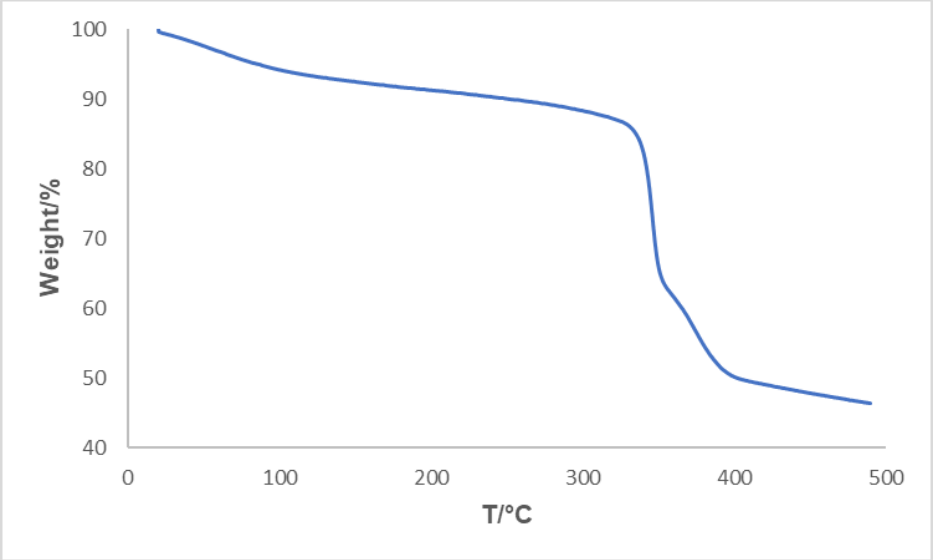

Figure 18: TGA curve of Cu-PgC_3.

2.4 Zinc Seamed Dimeric Nanocapsules

Zinc seamed dimeric nanocapsules (Zn-PgC_3) were prepared based on the reported procedure, with slight modifications.[109] A solution of zinc nitrate hexahydrate in pyridine was sonicated until dissolved, then added to a methanolic solution of PgC_3. This resulted in the precipitation of a yellow powder, which was collected by vacuum filtration. The product was characterised by ^{1}H and ^{13}C proton decoupled NMR spectroscopy and TGA.

The ^{1}H NMR spectrum (partially shown in Figure 19) confirmed the structure of Zn-PgC_3. Integration of the NMR resonances suggest that the MONC consists of two PgC_3 ligands seamed together by eight zinc(II) ions, along with a single pyridine molecule encapsulated in the cavity. Resonances at 0.98, 1.34, 2.19 and 4.19 ppm were assigned to the -CH_3, -CH_2, -CH_2 and -CH hydrogen atoms of the alkyl substituents, respectively. Three pyridyl hydrogen atom resonances appear where expected in DMSO at 7.41, 7.81 and 8.58 ppm. However, three additional resonances appear significantly upfield (denoted with stars in Figure 21). Integration of these two sets of peaks revealed that these two types of pyridine molecules are present in an 8:1 ratio. This pattern is interpreted in terms of eight pyridine molecules coordinated to the zinc cations on the outside of the cavity and one encapsulated pyridine guest. This observation is in agreement with previous reports.[109] $^{13}C\{^{1}H\}$ NMR spectroscopy provides further support for this hypothesis. The observation of two sets of pyridyl resonances implies slow exchange on the NMR spectroscopic timescale and hence a kinetically stable capsule despite the relatively labile nature of zinc(II).

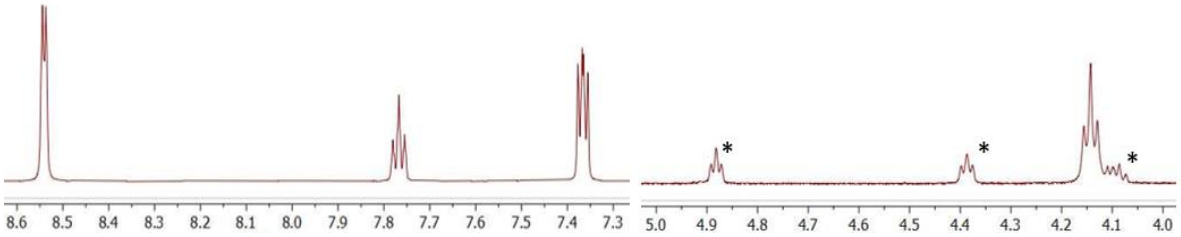

Figure 19: Partial ^{1}H NMR spectrum of Zn-PgC_3. Stars denote the resonances assigned to the encapsulated pyridine molecule. These signals experience a significant upfield shift as a result of the shielding effect of the aromatic rings of the cavity wall.

Diffusion-ordered NMR spectroscopy (DOSY) was used to verify the encapsulation of the pyridine molecule. Zn-PgC_3 was expected to have a smaller diffusion constant compared to that of solvent molecules and coordinated pyridine ligands outside of the cavity. It was found that the high field resonances corresponding to the encapsulated pyridine molecule had a similar diffusion coefficient to that of the PgC_3 ligands that comprise the MONC. In addition, the diffusion coefficient values of the encapsulated pyridine and PgC_3 ligands were significantly smaller compared to the pyridine ligands outside of the cavity. The spectrum also shows multiple diffusion coefficient signals for the ligated pyridyl hydrogen atoms (signals sets between 7 to 9 ppm). This suggests that the coordinated pyridine molecules outside of the cavity could be actively in exchange.

The diffusion coefficient values obtained from DOSY NMR were also used to estimate the molecular weight of Zn-PgC_3 to confirm whether the Zn MONC holds together in solution. This was performed based on the work by Morris *et al.* who proposed a model to roughly estimate the molecular mass of a compound based on its diffusion coefficient values.[119] There are slight deviations between diffusion coefficient values of Zn-PgC_3. For example, the propyl alkyl tail -CH_3, -CH_2 and -CH_2 hydrogen atoms of PgC_3 have diffusion coefficient values of $1.09x10^{-10}$, $1.10x10^{-10}$ and $1.11x10^{-10}$ m^2 sec^{-1}, respectively. These values yield an estimated molecular weight of 2422.1, 2369.4 and 2318.4 g mol^{-1}, respectively. Assuming full occupancy of Zn-PgC_3 based on the ^{1}H and ^{13}C NMR results, the true molecular weight of Zn-PgC_3 can be calculated to 2447.32g mol^{-1}. Thus, the estimated molecular weight from DOSY is very similar to the theoretical molecular weight. The molecular weight derived from DOSY NMR is an approximation and does not account for factors such as shape, solvation and concentration. However, the close agreement between

the DOSY and theoretical molecular weight values implies that Zn-PgC_3 retains its structure in solution.

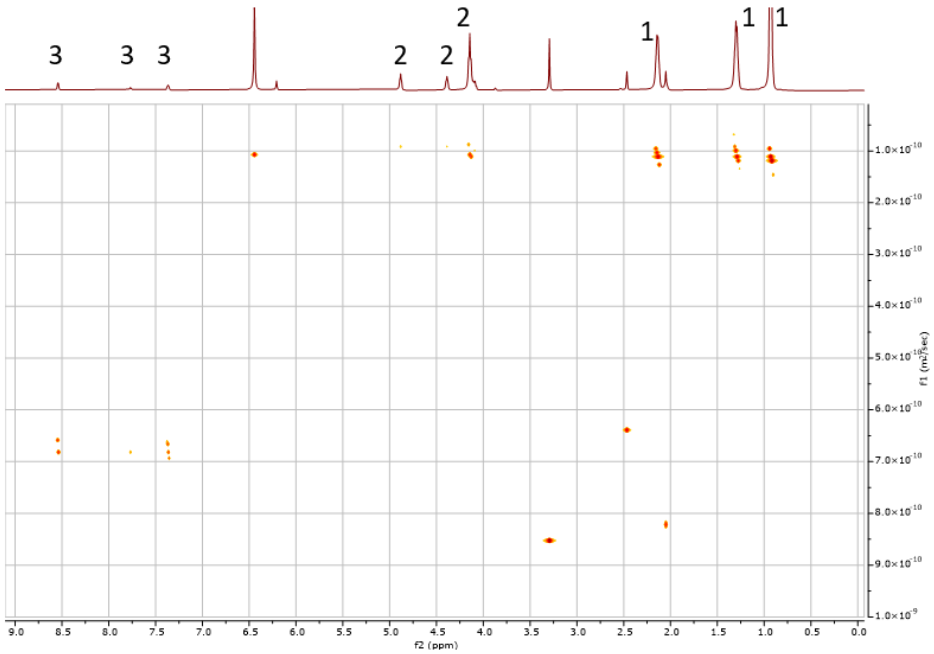

Figure 20: DOSY Transform NMR spectrum of Zn-PgC_3. Peaks are labelled as following: 1 – alkyl substituents of PgC_3, 2 – encapsulated pyridine and 3 – free pyridine. Other peaks are that of solvent molecules or hydrogen atoms of PgC_3.

The thermal stability of Zn-PgC_3 was evaluated using TGA. This was performed under nitrogen environment whilst heating the compound from room temperature to 500°C. The thermogram (Figure 21) reveals a weight loss of 1.4% up to 188°C, which could be the result of solvent loss from the powder. The decomposition onset temperature is 188°C, which is significantly lower compared to PgC_3 and Cu-PgC_3. Nonetheless, this thermal stability is high enough for the purpose of preparing PLs. The weight loss is relatively linear as the temperature is increased, and a 37.1% decrease in weight is observed. The axially coordinated pyridine ligands make up approximately 26% of the weight of the MONC. Thus, this weight loss can be attributed to a more significant decomposition than loss of the pyridine ligands. It is most likely that further increase in temperature would result in more decrease in weight as the full decomposition of Zn-PgC_3 is not observed on the thermogram.

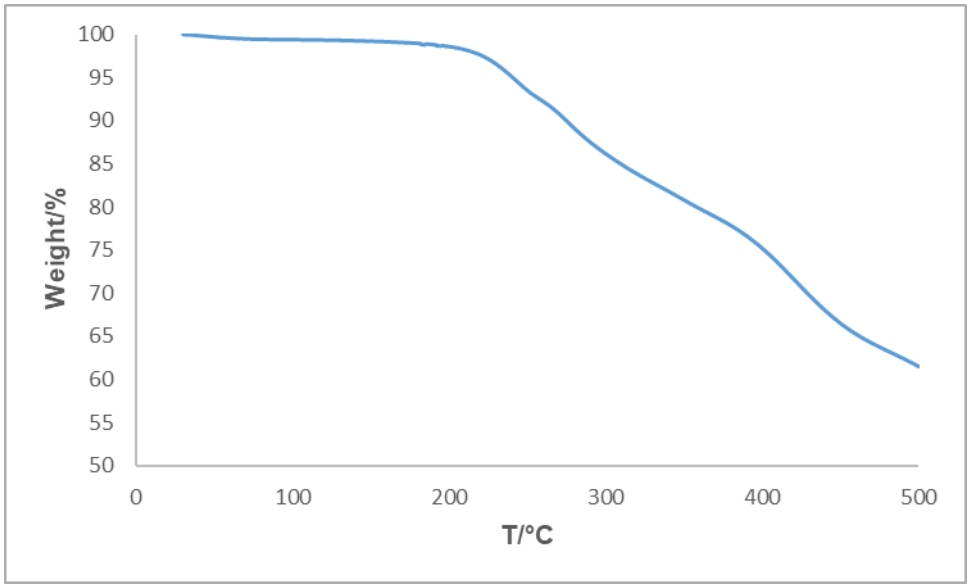

Figure 21: TGA curve of Zn-PgC$_3$.

2.5 Guest Exchange of Zinc Seamed Dimeric Nanocapsules

Recently, a coordination cage was subjected to liquid state and gas diffusion guest encapsulation experiments, monitored *via* NMR spectroscopy.[99] Upon successful encapsulation, the NMR spectrum exhibited an upfield shift of the encapsulated guest resonances relative to the free guest resonances. Thus, similar shifts were expected to be observed upon successful guest exchange in this work.

Guest exchange was performed on Zn-PgC$_3$ MONCs due to their high thermal stability and the diamagnetic nature of zinc(II), which means that changes in the environment of the capsule can be monitored *via* ^{1}H NMR spectroscopy. The experiments were performed in the liquid state and *via* gas diffusion. For the former, a 2 mM solution of Zn-PgC$_3$ in deuterated dimethyl sulfoxide (d$_6$-DMSO) was prepared in an NMR tube. To that, 10 µL of the guest (1-propanol, 1-butanol, isobutanol, and toluene) was added. These guests were selected due to their varying size and shape. Each mixture was equilibrated for 18 hours, after which the ^{1}H NMR spectra were acquired. For the gas diffusion experiments, 2 mg of solid Zn-PgC$_3$ was placed in a vial, which was set inside a larger vial containing 1 mL of the guest (benzene, toluene, chloroform and dichloromethane). Again, these guests were selected due to their varying size and shape along with their volatile nature. The larger vial was capped and left to equilibrate for 24 hours. The Zn-PgC$_3$ powder was then dissolved in d$_6$-DMSO and taken for ^{1}H NMR spectroscopy.

The ^{1}H NMR spectra of the liquid state experiments showed the presence of resonances assigned to the newly added potential guests. However, no upfield shifts were observed for the guest molecule resonances, indicating that they have not entered the cavity of Zn-PgC$_3$. Gas diffusion experiments showed similar results – all guest resonances were observed where expected in d_6-DMSO without the appearance of any shifts that would suggest that guest molecules were encapsulated. Figure 22 shows the ^{1}H NMR spectrum of Zn-PgC$_3$ with dichloromethane. The hydrogen atom resonance of dichloromethane is observed at 5.77 ppm, which is where it is expected to appear in d_6-DMSO. No upfield shifts corresponding to this resonance are observed, leading to the conclusion that dichloromethane does not enter the Zn-PgC$_3$ cavity. However, the presence of this resonance suggests some type of host-guest interaction, resulting in the absorption of the guest molecules onto the surface of Zn-PgC$_3$.

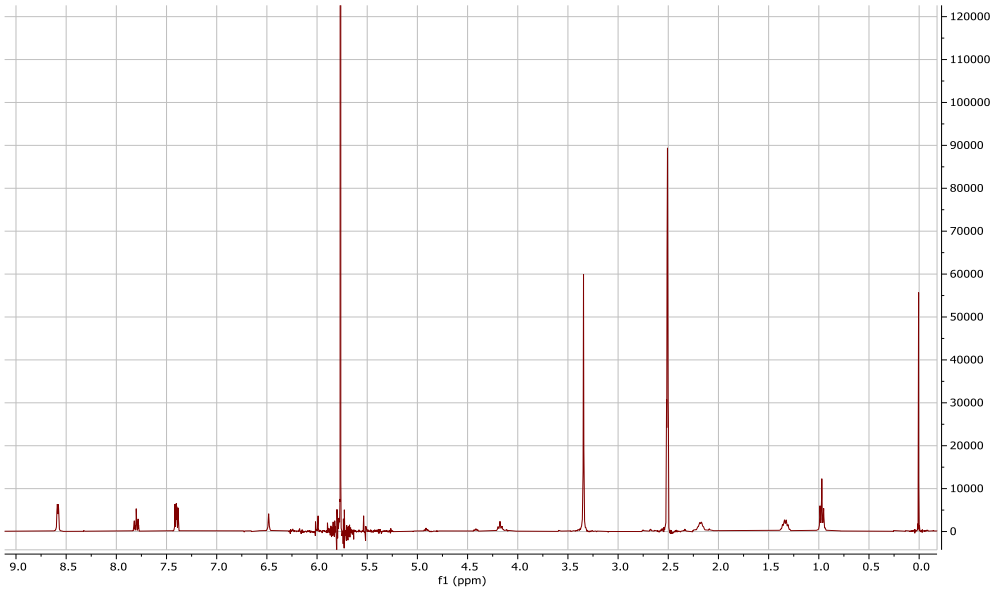

Figure 22: ^{1}H NMR spectrum of Zn-PgC$_3$ after gas diffusion with dichloromethane.

Furthermore, the resonances previously assigned to the encapsulated pyridine molecule (Figure 19) remained, further indicating that no host-guest exchange has occurred. In Figure 24, these resonances are observed between 4 and 5 ppm. Even though the guest molecules are small enough to fit through the window, the occupied cavity experiences significant restrictions. The cavity volume of Zn-PgC$_3$ is approximately 141 Å^3, of which 75.1 Å^3 is taken up by the encapsulated pyridine, leaving minimal space to bind other

molecules.[109] In addition, even though calculations indicate that pyridine could be small enough to exit the cavity, then in reality this does not occur.

Overall, these results show that the selected guest molecules do not participate in guest exchange with pyridine inside the MONC. The ^{1}H NMR spectra clearly show that pyridine does not leave the cavity of Zn-PgC$_3$. Subsequently, the cavity volume is too small to be occupied by other guests. However, the presence of guest resonances in the ^{1}H NMR spectra indicates some host-guest interactions. This could be the result of the interactions between the newly added guests and ligated pyridine molecules, resulting in the absorption of the guests onto the surface of Zn-PgC$_3$.

2.6 Metal-Organic Frameworks

This work discusses the use of Basolite® F300 MOF for the preparation of Type 3 porous liquids (PL). The prepared PL will be tested for dye absorption efficiency. This technique has been selected as it can be used for the determination of empty spaces within the ionic liquids. For instance, an aqueous dye solution can be added to the PL colloid. If the prepared colloid is stable and capable of dye uptake, the dye will permeate from the aqueous phase to the PL phase. This results in the colour change of the aqueous solution which means that the kinetics of this change can be monitored via UV-Vis spectroscopy. This gives the opportunity to quantify the efficiency of the PL. Furthermore, if successful, the as-prepared PLs could be potentially used for wastewater remediation purposes.

2.6.1 Basolite® F300

Basolite® F300 (BF300), empirical formula $C_9H_3FeO_6$, was purchased from Merck and characterised *via* TGA and PXRD. This MOF is prepared commercially using an electrochemical method resulting in a brown amorphous powder.[120] XANES and EXAFS studies have concluded that BF300 consists of Fe^{3+} ions coordinated to the 1,3,5-benzenetricarboxylic acid with the ligands arranged in an octahedral geometry.[121] TGA results reveal an initial weight loss of approximately 15.6% by 105.4°C, which is most likely the decomposition of residual solvent. The decomposition onset temperature of the framework is 340.7°C, accompanied by a 45.5% weight loss. These values are in agreement with previous reports.[122,123] Figure 23 shows the PXRD pattern of BF300. The pattern contains broad peaks and low resolution, which can be attributed to the disordered nature of the framework and the small crystallite size. The Scherrer equation is used to estimate the

average crystallite size, which was calculated to be 7.4 nm, in accurate agreement with previous reports.[122,123]

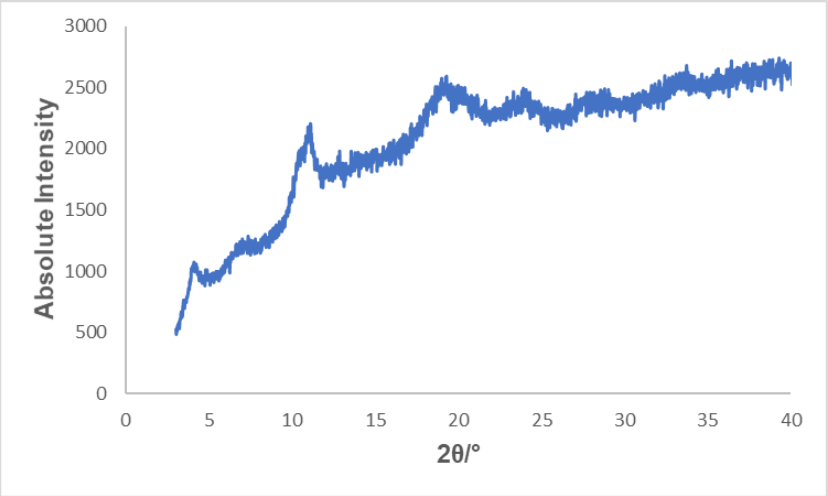

Figure 23: X-ray powder diffraction pattern of Basolite F300.

The absorption capability of BF300 was tested on two anionic dyes, Alizarin Red S (ARS) and Acid Blue 25 (AB25) (Figure 24). A specific amount of absorbent was stirred in each aqueous dye solution for 24 hours to confirm absorption of dyes. After the addition of BF300 to aqueous solutions of ARS and AB25, it was determined that the MOF is capable of ARS absorption. The solution containing AB25 changed from blue to green and remained as such. The green colour is the result of the pH drop to approximately 5.5. More importantly, it was determined that BF300 is not capable of efficient absorption of the AB25 dye. Thus, AB25 was not used for the evaluation of the uptake efficiency of the porous liquids.

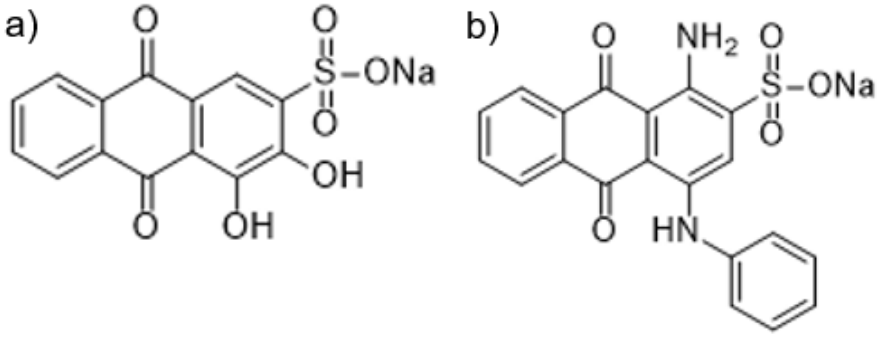

Figure 24: Structures of a) Alizarin Red S and b) Acid Blue 25.

The porous liquids (PLs) were prepared by adding 10 mg of BF300 to 1 mL of each ionic liquid (IL), shown in Figure 25. The resulting mixture was sonicated until a well-dispersed brown-orange colloid formed. The resulting colloids were tested for dye absorption

capabilities by adding 1 mL of an aqueous ARS to 1 mL of each PL. The resulting mixture contained two phases (aqueous dye phase and the ionic liquid phase containing BF300) and the dye permeation from the aqueous to the PL phase was monitored for 24 hours.

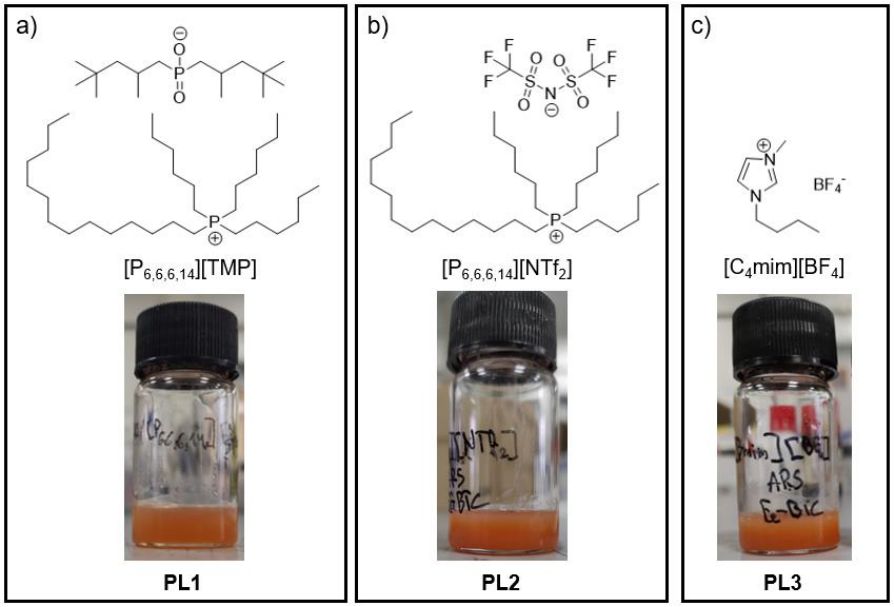

Figure 25: Ionic liquids used for the preparation of porous liquids by the addition of 10 mg of BF300 and sonication until the formation of the brown colloids shown below. a) Trihexyltetradecylphosphonium bis(2,4,4-trimethylpentyl)phosphinate and the resulting porous liquid **PL1**. b) Trihexyltetradecylphosphonium bis(trifluoromethylsulfonyl)amide and the resulting porous liquid **PL2**. c) 1-butyl-3methyl-imidazolium tetrafluoroborate and the resulting porous liquid **PL3**.

The stability of the PLs was evaluated by monitoring the solutions visually. It was hypothesised that less stable PLs would exhibit precipitation of BF300 faster compared to more stable PLs. Within 24 hours, **PL3** displayed such behaviour as the mixture became clear and BF300 had precipitated out of the IL. As for **PL1** and **PL2**, these mixtures retained stability for several days. This leads to the assumption that the hydrophobic interactions between BF300 and the phosphonium-based ILs lead to higher stability of the resulting PLs while the hydrophilic nature of $[C_4mim][BF_4]$ does not provide solution stabilizing interactions.

Figure 26 shows dye permeation into **PL1**, **PL2** and **PL3**. Within 24 hours, most of the dye has permeated form the aqueous phase into the ionic liquid phase of **PL1** and **PL2**. This could suggest that porous liquids have been successfully prepared. However, when this was repeated with pure ILs, the same phenomenon occurred. It has been determined that the

extraction of dyes from aqueous solutions is performed *via* anion exchange between the anionic dye and the IL anion.[124] This mechanism is likely to exist in the presence of BF300 within the ionic liquid. On the other hand, **PL3** does not form a stable colloid but rather forms a homogeneous solution with the aqueous phase. This was observed for the mixtures without BF300, which suggests that **PL3** is unstable, resulting in the precipitation of BF300.

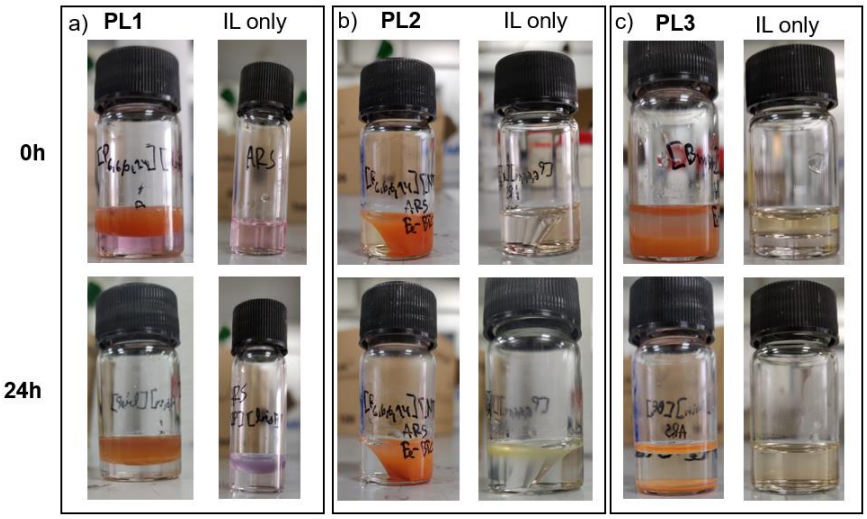

Figure 26: Permeation of Alizarin Red S from the aqueous solution into pure ionic liquids and ionic liquids containing BF300. a) Pure [C_4mim][BF_4] and **PL1** with ARS. b) Pure [$P_{6,6,6,14}$][NTf_2] and **PL2** with ARS. c) Pure [$P_{6,6,6,14}$][TMP] and **PL3** with ARS.

UV-Vis spectroscopy was used to compare dye uptake capabilities of **PL1** and **PL2** to their pure ionic liquid counterparts. Briefly, five solutions consisting of 1 mL of ILs and PLs were prepared. To each, 3 mL of 50µM aqueous ARS was added, resulting in a bilayer formation. At specific time points, the aqueous layers were removed and their UV-Vis spectra obtained. Figure 27 shows the dye uptake efficiency for [$P_{6,6,6,14}$][NTf_2] (labelled as pure IL) and **PL2**. This shows that there does not seem to be a significant difference between the IL and PL efficiencies toward dye absorption. On one hand, this suggests that there might not be intrinsic porosities present within **PL2**. On the other, if dye absorption is governed by anion exchange, it is plausible that dye molecules will stay in solution *via* noncovalent interaction with the phosphonium cation by potentially forming an ionic bond. This would prevent the dye molecules from entering the pores of BF300. This experiment was also performed with [$P_{6,6,6,14}$][TMP], but as the aqueous layer formed below the IL layer, it was difficult to obtain enough sample for UV-Vis analysis. This resulted in flat spectra for certain time points, which made data analysis impossible.

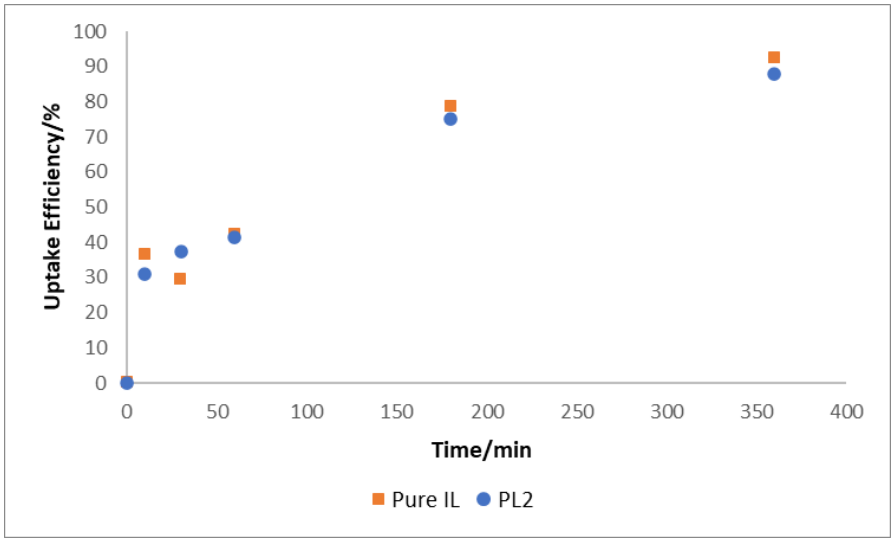

Figure 27: Dye uptake efficiency of $[P_{6,6,6,14}][NTf_2]$ (pure IL) and **PL2**.

Overall, it is rather difficult to confirm the presence of permanent porosity in the IL phase without further experiments. Using UV-Vis spectroscopy to study the absorption intensity changes within the aqueous phase could be effective. Overall, due to the inconclusive nature of these results, it is difficult to determine whether the prepared **PL1** and **PL2** are permanently porous liquids as more work is required.

3. Future Work

Future work would heavily include further characterisation techniques for **PL1** and **PL2**. By definition, porous liquids must contain empty spaces provided by the pore generator – *i.e.*, Basolite F300 MOF in this work. Positron annihiliation lifetime spectroscopy (PALS) has been proven to be one of the most efficient pore characterisation methods. This technique would allow for the accurate determination of empty pore networks of Basolite F300 along with the determination of the pore sizes. On the other hand, if the solvent molecules occupy the pore spaces, this could be confirmed *via* PALS as smaller pore values would be obtained. This technique could be coupled with rheology studies, which could further assess the stability and fluid-like behaviour of the PLs. In addition, the potential application of Cu-PgC_3 as Type 2 PLs could be undertaken by applying similar characterisation methods to evaluate their porosity and stability.

More quantitative results for **PL1** and **PL2** could be obtained by using smaller molecules than the dyes mentioned in this work. For instance, various gases (N_2, O_2 or CO_2) could be bubbled through the PLs for a specific amount of time. Subsequently, FT-IR spectra could be obtained to confirm any adsorption of gas molecules. Coupling these techniques with aforementioned characterisation techniques would provide a full picture to effectively evaluate the porosity and efficiency of the prepared porous liquids.

4. Conclusions

This work describes the preparation of porous liquids of Type 2 and 3 using metal-organic nanocapsules and metal-organic frameworks, respectively. The main challenge regarding the preparation of Type 2 porous liquids was ensuring the cavities of the capsules were empty of solvent molecules. This challenge was not overcome as evidenced *via* NMR studies on Zn-PgC_3. Rather, it was confirmed that guest exchange of pyridine with smaller molecules was unsuccessful.

Three Type 3 PLs (**PL1**, **PL2**, and **PL3**) were prepared. **PL1** and **PL2** exhibited superior stability compared to **PL3** and remained stable colloids for days. All PLs were evaluated qualitatively for dye absorption using a biphasic setup. It was shown that dyes permeated from the aqueous phase to the ionic liquid phase leaving the former transparent. This is most likely due to the anion exchange between the IL anion and the anionic dye in the aqueous phase. UV-Vis results showed that **PL2** has a similar dye uptake efficiency compared to the IL that it is composed of. This suggests that there is no intrinsic porosity within this PL. However, it could also be argued that if dye absorption mechanism is governed by anion exchange, then the dye molecules will stay in solution *via* noncovalent attraction forces and will not enter the pores of BF300.

5. Experimental

5.1 Synthesis and Materials

All starting materials were purchased from Merck and used without further purification. All ionic liquids were purchased from Merck and used without further treatment or purification. ^{1}H and $\{^{1}H\}^{13}C$ NMR spectra were obtained using the Bruker Avance III-HD-400 spectrometer with operating frequency of 400.07 MHz. DOSY NMR spectra were obtained using the Varian VNMRS-700 spectrometer with operating frequency of 699.73 MHz. Chemical shifts are relative to internal TMS. FT-IR spectra were obtained using the PerkinElmer Spectrum 100 series spectrometer in the range of 4000 cm^{-1} to 550 cm^{-1} at a resolution of 0.5 cm^{-1}. Three spectra of each sample were obtained, and the average was plotted. PXRD patterns were measured using the Bruker AXS D8 Advance in Bragg-Brentano geometry, equipped with a Lynxeye Soller PSD detector. Samples were measured on a Si low background sample holder and analysed using Cu-Kα radiation at a wavelength of 1.5406 Å. Samples were scanned over an angle range of 2-30° 2θ with a step size of 0.02° and a scan rate of 1s per step. Crystallite size analysis was performed using the equation below:

$$D = \frac{K\lambda}{\tau cos\theta_B} \quad (1)$$

Where D is the crystallite size, τ is full-width at half maximum, K is a constant close to unity (0.9 was used in this work), λ is the X-ray wavelength, and θ_B is the Bragg angle. MALDI-MS spectra were acquired using the Autoflex II ToF/ToF mass spectrometer (Bruker Daltonik GmBH), equipped with a 337 nm nitrogen laser. The linear mode of analysis was used between *m/z* 1097.0 to 9663.3. Trans-2-[3-(4-tert-Butylphenyl)-2-methyl-2-propenylidene]malononitrile (DCTB) was used as the matrix. Prior to the analysis, 1μL of the sample was placed onto a metal target and allowed to evaporate. TGA spectra were obtained using the Perkin Elmer Pyris I thermogravimetric analyser and DSC was performed using the Q1000 DSC from TA Instruments. Samples were run from room temperature up to designated temperatures under nitrogen, helium or oxygen atmosphere. Elemental analysis was performed with the Exeter CE-440 Elemental Analyser and all analysed samples were dried prior to analysis using the Abderhalden's drying pistol under toluene reflux. UV-Vis spectra were recorded using the Cary 5000 UV-Vis-NIR spectrophotometer with 1 nm resolution.

5.2 Synthesis of C-propylpyrogallol[4]arene

The procedure to prepare *C*-propylpyrogallol[4]arene was taken from the work of Gerkensmeier *et al*.[125] Pyrogallol (5.00 g, 39.6 mmol) was added to a solution of ethanol (30 mL) and concentrated hydrochloric acid (6 mL). To the resulting mixture, 1 eq. of aldehyde was added dropwise under ice. The mixture was heated under reflux for 24h after which the reaction was cooled to room temperature and the precipitate, white powder, was vacuum filtered and washed with cold ethanol, then recrystallised from methanol. The product was characterised by SXRD, ^{1}H and proton decoupled ^{13}C NMR. Yield = 1.50 g, 2.1 mmol, 21%.

^{1}H NMR (400 MHz, acetone-d_6): δ = 0.96 (12H, t, *J* = 7.4 Hz, CH_3), 1.26 – 1.40 (8H, m, CH_2), 2.22 – 2.33 (8H, m, CH_2), 3.32 (4H, s, CH), 4.37 (4H, t, *J* = 8.0 Hz, ArH), 7.14 (4H, s, ArH), 7.21 (4H, s, OH), 8.12 (8H, s, OH).

{^{1}H}^{13}C NMR (101 MHz, acetone-d_6) δ = 13.42, 20.96, 33.72, 35.00, 113.64, 124.84, 132.78, 139.23.

5.3 Synthesis of metal-seamed nanocapsules

5.3.1 Mg-seamed hexameric nanocapsules

The Mg-seamed hexameric MONCs were prepared based on the synthesis described by Atwood *et al*.[126] *C*-propylpyrogallol[4]arene (360 mg, 0.5 mmol) and $Mg(NO_3)\cdot 6H_2O$ (513 mg, 2.0 mmol) were dissolved in 5 mL of DMF and 5 mL MeCN. To this mixture, 500µL of deionized water and imidazole (0135 mg, 2.0 mmol) were added. The mixture was sonicated for 5 minutes resulting in a dark blue solution, which was heated at 100°C overnight. Plate-like crystals were collected by vacuum filtration and characterised by SXRD. Yield = 0.22 g, 0.040 mmol, 48% based on the formula $C_{240}H_{318}Mg_{24}O_{120}$.

5.3.2 Cu-seamed hexameric nanocapsules

Cu-seamed hexameric MONCs were prepared *via* a known procedure.[108] By adding methanolic $Cu(NO_3)_2\cdot 2.5H_2O$ (40 mM) to a methanol solution of PgC_3 (10 mM), the instantaneous formation of a brown precipitate was observed. To obtain the product, the precipitate was vacuum filtered and characterized by TGA, MALDI MS and elemental analysis. Yield = 0.066 g, 0.011 mmol, 69% based on the formula $Cu_{24}C_{246}H_{312}O_{102}$.

MALDI MS (*m*/*z*): 6409.3 $[M+H+24H_2O+6CH_3OH]^+$, 6443.8 $[M+H+24H_2O+7CH_3OH]^+$, 6473.6 $[M+H+24H_2O+8CH_3OH]$.

5.3.3 Zn-seamed dimeric nanocapsule

Zn-seamed dimeric MONCs were prepared *via* a known procedure, with slight modifications.[109] Zinc nitrate hexahydrate (0.1654 g, 0.56 mmol) was dissolved in 2 mL of pyridine, which was sonicated for 10 minutes. The resulting solution was mixed with a 4 mL methanol solution of PgC_3 (0.10 g, 0.139 mmol). A yellow precipitate was collected *via* vacuum filtration and characterised *via* TGA, ^{1}H and ^{13}C NMR. Yield = 0.10 g, 47%.

^{1}H NMR (400 MHz, DMSO-d_6): δ = 0.97 (24H, t, J = 7.4 Hz, CH_3), 1.33 (16H, p, J = 7.4 Hz, CH_2), 2.18 (16H, d, J = 7.4 Hz, CH_2), 4.12 (1H, t, J = 7.9 Hz, encapsulated pyridine) overlaying with 4.18 (8H, t, J = 8.0 Hz, CH), 4.43 (2H, t, J = 6.8 Hz, encapsulated pyridine), 4.93 (2H, dd, J = 6.8 Hz, 5.3 Hz, encapsulated pyridine), 6.49 (8H, s, ArH), 7.41 (16H, ddd, J = 7.6, 4.3, 1.5 Hz, pyridine), 7.81 (8H, tt, J = 7.6, 1.8 Hz, pyridine), 8.58 (16H, dt, J = 4.3, 1.8 Hz, pyridine). Obtained peaks are in close agreement with literature.[109]

{^{1}H}^{13}C NMR (101 MHz, DMSO-d_6): δ = 14.58, 21.53, 32.68, 35.54, 107.40, 124.39, 124.48, 125.35, 136.80, 139.31, 141.82, 150.06.

5.4 Dye adsorption

Two dyes, Acid Blue 25 and Alizarin Red S, were selected as adsorbates. Stock solutions of both dyes having 50μM concentration were prepared. To test the dye adsorption capability of Basolite F300, 0.1g of the adsorbent was added to 50 mL of dye solution. The mixture was stirred for 24 hours, then filtered to obtain the MOF. Porous liquid dye adsorption was performed *via* a two-phase method. 1 mL of ionic liquid including 10 mg of BF300 was stirred until a homogeneous colloid was obtained. To this, 1 mL of dye solution was added, which resulted in the formation of two phases. The mixture was allowed to equilibrate for 24 hours. For UV-Vis analysis, samples were prepared by adding 3 mL of aqueous dye solution to 1 mL of either IL only or PL colloid. Samples were collected at t = 0, 10, 30, 60, 180, and 360 min. time points by removing the aqueous layer with a Pasteur pipette. One sample was prepared for each time point.

5.5 Analysis

5.5.1 Gas diffusion of VOCs

The inclusion of VOCs into the Zn MONCs was studied by ^{1}H NMR spectroscopy. A small vial containing 2 mg of the Zn MONC was placed in a larger vial containing 1 mL of the guest VOC, which was then capped and sealed tightly. Four such vials containing toluene,

chloroform, dichloromethane and benzene as VOCs were prepared. The samples were equilibrated for 24 hours, then prepared for NMR spectroscopy.

^{1}H NMR (400 MHz, DMSO-d_6, benzene VOC): δ = 0.97 (24H, t, *J* = 7.2 Hz), 1.32 (16H, p, *J* = 7.3 Hz), 2.18 (14H, d, *J* = 7.7 Hz), 4.11 (1H, t, *J* = 7.7 Hz, **enc. pyridine**), 4.18 (8H, t, *J* = 7.9 ,), 4.42 (2H, t, *J* = 6.8H, **enc. pyridine**), 4.89 – 4.95 (2H, m, **enc. pyridine**), 6.48 (6H, s), 7.37 (132H, s, **benzene**), 7.80 (7H, *J* = 7.60, 1.80 Hz), 8.58 (14H, dt, *J* = 4.4, 1.8 Hz).

^{1}H NMR (400 MHz, DMSO-d_6, $CHCl_3$ VOC): δ = 0.93 – 1.00 (24H, m), 1.33 (16H, q, *J* = 7.4 Hz), 2.18 (14H, d, *J* = 7.8 Hz), 4.11 (1H, t, J = 7.9 Hz, **enc. pyridine**), 4.18 (8H, t, *J* = 7.9 Hz), 4.42 (2H, t, *J* = 6.9 Hz, **enc. pyridine**), 4.91 (2H, t, *J* = 6.1 Hz, **enc. pyridine**), 6.48 (6H, s), 7.40 (15H, ddd, *J* = 7.6, 4.3, 1.5 Hz), 7.80 (8H, tt, *J* = 7.6, 1.9 Hz), 8.33 (50H, s, **$CHCl_3$**), 8.55 – 8.62 (15H, m).

^{1}H NMR (400 MHz, DMSO-d_6, CH_2Cl_2 VOC): δ = 0.97 (24H, t, *J* = 7.2 Hz), 1.33 (16H, q, *J* = 7.4 Hz), 2.12 – 2.23 (14H, m), 4.11 (1H, t, *J* = 7.6 Hz, **enc. pyridine**), 4.18 (8H, t, *J* = 8.0 Hz), 4.41 (2H, t, *J* = 6.8 Hz, **enc. pyridine**), 4.91 (1H, m, **enc. pyridine**), 5.77 (146H, s, **CH_2Cl_2**), 5.77 – 5.93 (8H, m), 6.48 (6H, s), 7.40 (15H, ddd, *J* = 7.6, 4.3, 1.5 Hz), 7.80 (8H, tt, *J* = 7.6, 1.8 Hz), 8.55 – 8.62 (14H, m).

^{1}H NMR (400 MHz, DMSO-d_6, toluene VOC): δ = 0.97 (24H, t, *J* = 7.3 Hz), 1.32 (16H, p, *J* = 7.3 Hz), 2.17 (15H, m) overlaying with 2.31(53H, d, *J* = 0.7 Hz, **toluene**), 4.11 (1H, t, J = 7.8 Hz, **enc. pyridine**), 4.18 (8H, t, *J* = 8.0 Hz), 4.42 (2H, t, *J* = 6.8 Hz, **enc. pyridine**), 4.89 – 4.94 (2H, m, **enc. pyridine**), 6.49 (7H, s), 7.11 – 7.20 (51H, m, **toluene**), 7.20 – 7.32 (37H, m, **toluene**), 7.40 (15H, ddd, *J* = 7.6, 4.3, 1.5 Hz), 7.80 (7H, tt, *J* = 7.6, 1.8 Hz), 8.58 (14H, dt, *J* = 4.3, 1.7 Hz).

5.6 Single Crystal X-ray Diffraction

Single Crystal X-ray diffraction was performed using the Bruker D8 Venture diffractometer (high intensity Mo/Cu dual IμS2 sources, CMOS area detector, 3 circle goniometer and focusing mirrors) at 120.0 K using Mo Kα radiation (λ = 0.71073 Å). The diffractometer is equipped with the Cryostream 700+ (Oxford Cryosystems) open flow nitrogen cryostat (temp. range 80 – 500 K) and HELIX (Oxford Cryosystems) open flow helium cryostat (temp. range 25 – 300 K). The structures were solved and refined using the Olex2 and SHELXTL softwares.

5.6.1 Single crystal X-ray diffraction data of PgC_3

Empirical formula	$C_{40}H_{48}O_{12}$ x 6 CH_3OH
Formula weight	913.03
Crystal system	triclinic
Space group	$P\bar{1}$
a (Å)	11.4710(7)
b (Å)	11.5460(7)
c (Å)	19.0494(12)
α (°)	75.464(2)
β (°)	74.498(2)
γ (°)	79.090(2)
Volume ($Å^3$)	2333.1(3)
Z	2
ρ_{calc} (g/cm^3)	1.300
μ (mm^{-1})	0.099
F(000)	984.0
Crystal size (mm^3)	0.22 × 0.17 × 0.08
2Θ range for data collection(°)	4.634 to 59
Index ranges	$-15 \leq h \leq 15$, $-15 \leq k \leq 15$, $-26 \leq l \leq 26$
Reflections collected	49603
Independent reflections	12972 [R_{int} = 0.0651, R_{sigma} = 0.0941]
Data/restraints/parameters	12972/0/854
Goodness-of-fit on F^2	1.019
Final R indexes [I>=2σ (I)]	R_1 = 0.0556, wR_2 = 0.1167
Final R indexes [all data]	R_1 = 0.1042, wR_2 = 0.1337
Largest diff. peak/hole (e $Å^{-3}$)	0.32/-0.29

5.6.2 Single crystal X-ray diffraction data of Mg-PgC_3

Empirical formula	$C_{240}H_{318}Mg_{24}O_{120}$
Formula weight	5706.37

Crystal system	monoclinic
Space group	$C\bar{2}m$
a (Å)	28.622(5)
b (Å)	35.281(6)
c (Å)	21.974(7)
α (°)	90
β (°)	119.878(3)
γ (°)	90
Volume ($Å^3$)	19241(8)
Z	2
ρ_{calc} (g/cm^3)	0.985
μ (mm^{-1})	0.112
F(000)	6012.0
Crystal size (mm^3)	0.21 × 0.13 × 0.06
2Θ range for data collection/°	3.7 to 53
Index ranges	$-35 \leq h \leq 35$, $-44 \leq k \leq 44$, $-27 \leq l \leq 27$
Reflections collected	114050
Independent reflections	20279 [R_{int} = 0.3263, R_{sigma} = 0.3583]
Data/restraints/parameters	20279/1048/886
Goodness-of-fit on F^2	1.026
Final R indexes [I>=2σ (I)]	R_1 = 0.1458, wR_2 = 0.3763
Final R indexes [all data]	R_1 = 0.3049, wR_2 = 0.4450
Largest diff. peak/hole (e $Å^{-3}$)	0.83/-0.61

6. Appendix: Structure and Abbreviation of Ionic Liquids

Name	Chemical Structure	Abbreviation and reference
1-butyl-3-methylimidazolium hexafluorophosphate	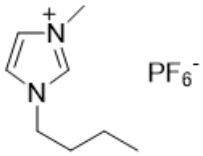	$[C_4mim]PF_6$], ref. 24
1-ethyl-3-methylimidazolium nitrate	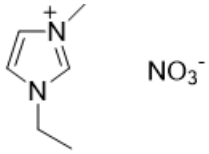	$[C_2mim][NO_3]$, ref. 15
1-butyl-3-methylimidazolium chloride	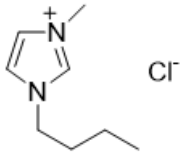	$[C_4mim][Cl]$, ref. 24
1-octyl-3-methylimidazolium hexafluorophosphate	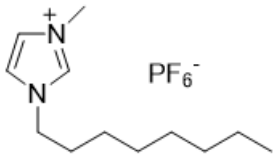	$[C_8mim][PF_6]$, ref. 23
1-butyl-3-methylimidazolium tetrafluoroborate	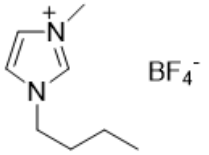	$[C_4mim][BF_4]$, ref. 35
1-ethyl-3-methylimidazolium bis(trifluoromethanesulfonyl)imide	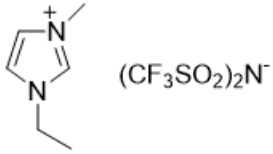	$[C_2mim][NTf_2]$, ref. 37
1-butyl-3-methylimidazolium bis(trifluoromethanesulfonyl)imide	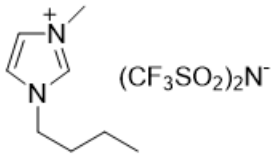	$[C_4mim][NTf_2]$, ref. 37
Tri(isobutyl) methylphosphonium tosylate	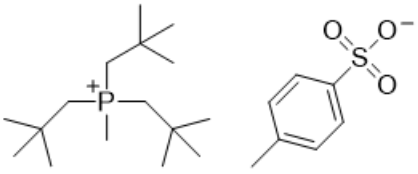	$[P_{i(444)1}][Tos]$, ref. 57

Tri(butyl) methylphosphonium methylsulfate	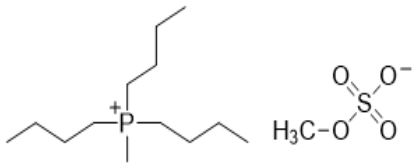	$[P_{4441}][CH_3SO_4]$, ref. 57
Tetraoctylphosphonium bromide	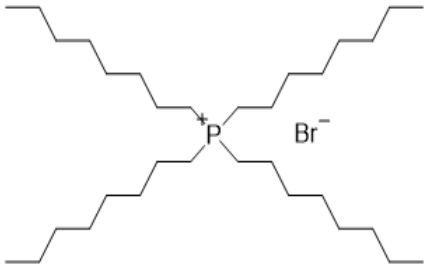	$[P_{8888}][Br]$, ref. 57
Tri(butyl) ethylphosphonium diethylphosphate	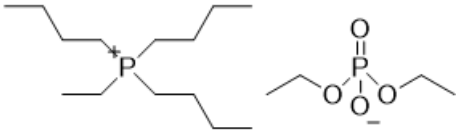	$[P_{4442}][(C_2H_5O)PO_2]$, ref. 57

References

1 G. Sethia and A. Sayari, *Carbon N. Y.*, 2016, **99**, 289–294.

2 M. X. Wu and Y. W. Yang, *Chinese Chem. Lett.*, 2017, **28**, 1135–1143.

3 S. Rashidi, J. A. Esfahani and A. Rashidi, *Renew. Sustain. Energy Rev.*, 2017, **73**, 1198–1210.

4 Y. Yang, J. Yu, A. Monemian Esfahani, K. Seiffert-Sinha, N. Xi, I. Lee, A. A. Sinha, L. Chen, Z. Sun, R. Yang and L. Dong, *Nanoscale*, 2018, **10**, 12704–12712.

5 M. I. Gonzalez, A. B. Turkiewicz, L. E. Darago, J. Oktawiec, K. Bustillo, F. Grandjean, G. J. Long and J. R. Long, *Nature*, 2020, **577**, 64–68.

6 L. Zou, Y. Sun, S. Che, X. Yang, X. Wang, M. Bosch, Q. Wang, H. Li, M. Smith, S. Yuan, Z. Perry and H. C. Zhou, *Adv. Mater.*, 2017, **29**, 1–35.

7 N. O'Reilly, N. Giri and S. L. James, *Chem. - A Eur. J.*, 2007, **13**, 3020–3025.

8 N. Giri, M. G. Del Pópolo, G. Melaugh, R. L. Greenaway, K. Rätzke, T. Koschine, L. Pison, M. F. C. Gomes, A. I. Cooper and S. L. James, *Nature*, 2015, **527**, 216–220.

9 E. Skoronski, M. Fernandes, F. J. Malaret and J. P. Hallett, *Sep. Purif. Technol.*, 2020, **248**, 117069.

10 L. Xue, E. Gurung, G. Tamas, Y. P. Koh, M. Shadeck, S. L. Simon, M. Maroncelli and E. L. Quitevis, *J. Chem. Eng. Data*, 2016, **61**, 1078–1091.

11 P. Walden, *Bull. l'Académie Impériale des Sci. St.-pétersbg.*, 1914, 405–422.

12 M. Deetlefs, M. Fanselow and K. R. Seddon, *RSC Adv.*, 2016, **6**, 4280–4288.

13 J. H. Shipp, *United States Pat. Off.*, 1939, 1–3.

14 M. Armand, F. Endres, D. F. MacFarlane, H. Ohno and B. Scrosati, *Nat. Mater.*, 2009, **8**, 621–629.

15 J. S. Wilkes and M. J. Zaworotko, *J. Chem. Soc. Chem. Commun.*, 1992, 965–967.

16 A. Berthod, M. J. Ruiz-Ángel and S. Carda-Broch, *J. Chromatogr. A*, 2018, **1559**, 2–16.

17 D. Czuryszkiewicz, A. Maćkowiak, K. Marcinkowska, A. Borkowski, Ł. Chrzanowski and J. Pernak, *Chempluschem*, 2019, **84**, 268–276.

18 R. Ratti, *Adv. Chem.*, 2014, **2014**, 1–16.

19 D. M. Piper, T. Evans, K. Leung, T. Watkins, J. Olson, S. C. Kim, S. S. Han, V. Bhat, K. H. Oh, D. A. Buttry and S. Lee, *Nat. Commun.*, 2015, **6**, 1–10.

20 M. Kar, O. Tutusaus, D. R. MacFarlane and R. Mohtadi, *Energy Environ. Sci.*, 2019, **12**, 566–571.

21 N. Vucetic, P. Virtanen, A. Nuri, I. Mattsson, A. Aho, J. P. Mikkola and T. Salmi, *J. Catal.*, 2019, **371**, 35–46.

22 R. Tao, G. Tamas, L. Xue, S. L. Simon and E. L. Quitevis, *J. Chem. Eng. Data*, 2014, **59**, 2717–2724.

23 J. G. Huddleston, A. E. Visser, W. M. Reichert, H. D. Willauer, G. A. Broker and R. D. Rogers, *Green Chem.*, 2001, **3**, 156–164.

24 S. Carda–Broch, A. Berthod and D. W. Armstrong, *Anal. Bioanal. Chem.*, 2003, **375**, 191–199.

25 Y. Zhang, L. Xue, F. Khabaz, R. Doerfler, E. L. Quitevis, R. Khare and E. J. Maginn, *J. Phys. Chem. B*, 2015, **119**, 14934–14944.

26 T. Erdmenger, J. Vitz, F. Wiesbrock and U. S. Schubert, *J. Mater. Chem.*, 2008, **18**, 5267–5273.

27 I. Dinarès, C. Garcia De Miguel, A. Ibáñez, N. Mesquida and E. Alcalde, *Green Chem.*, 2009, **11**, 1507–1510.

28 H. L. Ngo, K. LeCompte, L. Hargens and A. B. McEwen, *Thermochim. Acta*, 2000, **357**–**358**, 97–102.

29 C. Kimble and C. M. Burba, *J. Phys. Chem. B*, 2017, **121**, 3099–3110.

30 M. G. Freire, A. R. R. Teles, M. A. A. Rocha, B. Schröder, C. M. S. S. Neves, P. J. Carvalho, D. V. Evtuguin, L. M. N. B. F. Santos and J. A. P. Coutinho, *J. Chem. Eng. Data*, 2011, **56**, 4813–4822.

31 Y. Shimizu, Y. Ohte, Y. Yamamura and K. Saito, *Chem. Phys. Lett.*, 2009, **470**, 295–299.

32 H. Abe, S. Tsuzuki and S. Ozawa, *Chem. Phys. Lett.*, 2018, **712**, 30–33.

33 B. Grüner, Z. Janoušek, B. T. King, J. N. Woodford, C. H. Wang, V. Všetečka and J. Michl, *J. Am. Chem. Soc.*, 1999, **121**, 3122–3126.

34 R. B. King, *Chem. Rev.*, 2001, **101**, 1119–1152.

35 B. Liu, R. Zhou, N. Bu, Q. Wang, S. Zhong, B. Wang and K. Hidetoshi, *J. Memb. Sci.*, 2017, **524**, 12–19.

36 C. Aucher, G. Guirado and E. Knipping, *New J. Chem.*, 2018, **42**, 4693–4699.

37 L. Mahrokh, H. Ghourchian, K. H. Nealson and M. Mahrok, *J. Mater. Chem. A*, 2017, **5**, 7979–7991.

38 F. Javed, F. Ullah, M. Razlan and H. Akil, *J. Mol. Liq.*, 2018, **271**, 403–420.

39 C. P. Fredlake, J. B. Crosthwaite, D. G. Hert, S. N. V. K. Aki and J. F. Brennecke, *J. Chem. Eng. Data*, 2004, **49**, 954–964.

40 M. Gorlov and L. Kloo, *J. Chem. Soc. Dalt. Trans.*, 2008, 2655–2666.

41 S. M. Nabavizadeh, H. Sepehrpour, H. R. Shahsavari and M. Rashidi, *New J. Chem.*, 2012, **36**, 1739–1743.

42 Y. Fang, P. Ma, H. Cheng, G. Tan, J. Wu, J. Zheng, X. Zhou, S. Fang, Y. Dai and Y. Lin, *Chem. - An Asian J.*, 2019, **14**, 4201–4206.

43 M. P. Cumplido, A. Cháfer, J. de la Torre and H. Poy, *J. Chem. Thermodyn.*, 2020, **140**, 105889.

44 J. K. Singh, R. K. Sharma, P. Ghosh, A. Kumar and M. L. Khan, *Front. Chem.*, 2018, **6**, 1–

12.

45 D. E. Kaufmann, M. Nouroozian and H. Henze, *Synlett*, 1996, 1091.

46 N. Karodia, S. Guise, C. Newlands and J. Andersen, *ChemComm*, 1998, 2341–2342.

47 J. Mcnulty, A. Capretta, J. Wilson, J. Dyck, G. Adjabeng, A. Robertson, N. Falls and T. Suzuki, *ChemComm*, 2002, 1986–1987.

48 M. P. Wylie, S. E. J. Bell, P. Nockemann, R. Bell and C. P. Mccoy, *ACS Omega*, 2020, **5**, 7771–7781.

49 L. Timperman, H. Galiano, D. Lemordant and M. Anouti, *Electrochem. commun.*, 2011, **13**, 1112–1115.

50 N. R. Ronco, C. Lancioni, L. M. Romero and C. B. Castells, *J. Chromatogr. A*, , DOI:10.1016/j.chroma.2020.461127.

51 J. Chen, M. Li, M. Li, X. Lin and T. Qiu, *ACS Sustain. Chem. Eng.*, 2020, **8**, 6956–6963.

52 L. M. dos Santos, F. L. Bernard, B. B. Polesso, I. S. Pinto, C. L. L. Frankenberg, M. Corvo, P. L. Almeida, E. Cabrita and S. Einloft, *J. Environ. Manage.*, 2020, **268**, [In press].

53 H. Mahandra, R. Singh and B. Gupta, *Sep. Purif. Technol.*, 2017, **177**, 281–292.

54 C. J. Bradaric, A. Downard, C. Kennedy, A. J. Robertson and Y. Zhou, *Green Chem.*, 2003, **5**, 143–152.

55 K. K. Thasneema, M. Shahin, T. Rosalin, K. K. Elyas, T. Dipin, P. K. Sahu, N. S. K. Kumar, V. C. Saheer, M. Messali and T. Ben, *J. Mol. Liq.*, 2020, **307**, 112960.

56 M. D. Green, C. Schreiner and T. E. Long, *J. Phys. Chem. A*, 2011, **115**, 13829–13835.

57 A. Bhattacharjee, J. A. Lopes-da-silva, M. G. Freire, J. A. P. Coutinho and P. J. Carvalho, *Fluid Phase Equilib.*, 2015, **400**, 103–113.

58 M. J. Earle and K. R. Seddon, *Pure Appl. Chem.*, 2000, **72**, 1391–1398.

59 M. Ke, A. Zhou, Z. Song and Q. Jiang, *Prog. Chem.*, 2007, **19**, 671–679.

60 M. Dong, L. Zhu, S. Zhu, J. Wang, J. Wang, H. Xie and Z. Du, *Chemosphere*, 2013, **91**, 1107–1112.

61 M. V. S. Oliveira, B. T. Vidal, C. M. Melo, R. de C. M. de Miranda, C. M. F. Soares, J. A. P. Coutinho, S. P. M. Ventura, S. Mattedi and Á. S. Lima, *Chemosphere*, 2016, **147**, 460–466.

62 E. Gomez-Herrero, M. Tobajas, A. Polo, J. J. Rodriguez and A. F. Mohedano, *Ecotoxicol. Environ. Saf.*, 2020, **187**, 109836.

63 A. Oskarsson and M. C. Wright, *Environ. Sci. Technol.*, 2019, **53**, 10539–10541.

64 N. Kundu, S. Roy, D. Mukherjee, T. K. Maiti and N. Sarkar, *J. Phys. Chem. B*, 2017, **121**, 8162–8170.

65 S. K. Ruokonen, C. Sanwald, A. Robciuc, S. Hietala, A. H. Rantamäki, J. Witos, A. W. T. King, M. Lämmerhofer and S. K. Wiedmer, *Chem. - A Eur. J.*, 2018, **24**, 2669–2680.

66 M. V. Fedotova, S. E. Kruchinin and G. N. Chuev, *J. Mol. Liq.*, 2019, 112081.

67 O. S. Hammond, D. T. Bowron and K. J. Edler, *Green Chem.*, 2016, **18**, 2736–2744.

68 V. Migliorati, F. Sessa and P. D'Angelo, *Chem. Phys. Lett. X*, 2019, **2**, 100001.

69 T. Moufawad, L. Moura, M. Ferreira, H. Bricout, S. Tilloy, E. Monflier, M. Costa Gomes, D. Landy and S. Fourmentin, *ACS Sustain. Chem. Eng.*, 2019, **7**, 6345–6351.

70 Y. Ji, Z. Meng, J. Zhao, H. Zhao and L. Zhao, *J. Chromatogr. A*, 2019, 460520.

71 J. Aldana-González, A. Sampayo-Garrido, M. G. Montes De Oca-Yemha, W. Sánchez, M. T. Ramírez-Silva, E. M. Arce-Estrada, M. Romero-Romo and M. Palomar-Pardavé, *J. Electrochem. Soc.*, 2019, **166**, D199–D204.

72 M. Faraji, *Microchem. J.*, 2019, **150**, 104130.

73 M. B. Haider, D. Jha, R. Kumar and B. Marriyappan Sivagnanam, *Int. J. Greenh. Gas Control*, 2020, **92**, 102839.

74 J. D. Mota-Morales, R. J. Sánchez-Leija, A. Carranza, J. A. Pojman, F. del Monte and G. Luna-Bárcenas, *Prog. Polym. Sci.*, 2018, **78**, 139–153.

75 J. Jiang, C. Yan, X. Zhao, H. Luo, Z. Xue and T. Mu, *Green Chem.*, 2017, **19**, 3023–3031.

76 J. S. Seo, D. Whang, H. Lee, S. I. Jun, J. Oh, Y. J. Jeon and K. Kim, *Nature*, 2000, **404**, 982–986.

77 L. Mi, H. Hou, Z. Song, H. Han, H. Xu, Y. Fan and S. W. Ng, *Cryst. Growth Des.*, 2007, **7**, 2553–2561.

78 C. E. Wilmer, O. K. Farha, Y. S. Bae, J. T. Hupp and R. Q. Snurr, *Energy Environ. Sci.*, 2012, **5**, 9849–9856.

79 P. Nugent, E. G. Giannopoulou, S. D. Burd, O. Elemento, E. G. Giannopoulou, K. Forrest, T. Pham, S. Ma, B. Space, L. Wojtas, M. Eddaoudi and M. J. Zaworotko, *Nature*, 2013, **495**, 80–84.

80 S. Hou, S. Razzaque and B. Tan, *Polym. Chem.*, 2019, **10**, 1299–1311.

81 D. W. Kim, S. M. Jung and H. Y. Jung, *J. Power Sources*, 2019, 227422.

82 Q. Q. Zhu, W. W. Zhang, H. W. Zhang, Y. Yuan, R. Yuan, F. Sun and H. He, *Inorg. Chem.*, 2019, **58**, 15637–15643.

83 X. Li, H. Xiong and Q. Jia, *ACS Appl. Mater. Interfaces*, 2019, **11**, 46205–46211.

84 C. Pi, C. Huang, Y. Yang, H. Song, X. Zhang, Y. Zheng, B. Gao, J. fu, P. K. Chu and K. Huo, *Appl. Catal. B Environ.*, 2019, 118358.

85 J. C. Groen, L. A. A. Peffer and J. Pérez-Ramírez, *Microporous Mesoporous Mater.*, 2003, **60**, 1–17.

86 B. Nie, X. Liu, L. Yang, J. Meng and X. Li, *Fuel*, 2015, **158**, 908–917.

87 X. Huang and Y. P. Zhao, *J. Pet. Sci. Eng.*, 2017, **159**, 197–204.

88 E. P. Barrett, L. G. Joyner and P. P. Halenda, *J. Am. Chem. Soc.*, 1951, **73**, 373–380.

89 J. Landers, G. Y. Gor and A. V. Neimark, *Colloids Surfaces A Physicochem. Eng. Asp.*, 2013, **437**, 3–32.

90 R. Yang, S. He, Q. Hu, M. Sun, D. Hu and J. Yi, *Fuel*, 2017, **197**, 91–99.

91 T. Zhang, S. Wei, G. I. N. Waterhouse, L. Fu, L. Liu, W. Shi, J. Sun and S. Ai, *Powder Technol.*, 2020, **360**, 55–64.

92 J. Liang, Y. Ling, X. wen Wu, H. A. Acciari and Z. Zhang, *J. Appl. Electrochem.*, 2019, **49**, 1211–1226.

93 X. Xiao, Y. Wang, H. Cheng, Y. Cui, Y. Xu, T. Yang, D. Zhang and X. Xu, *Mater. Chem. Phys.*, 2020, **240**, 122202.

94 T. I. Shabatina, O. I. Vernaya, A. V. Nuzhdina, V. P. Shabatin, A. M. Semenov and M. Y. Mel'nikov, *Russ. J. Phys. Chem. A*, 2019, **93**, 1970–1975.

95 A. Bavykina, A. Cadiau and J. Gascon, *Coord. Chem. Rev.*, 2019, **386**, 85–95.

96 S. He, L. Chen, J. Cui, B. Yuan, H. Wang, F. Wang, Y. Yu, Y. Lee and T. Li, *J. Am. Chem. Soc.*, 2019, jacs.9b08458.

97 R. Gaillac, P. Pullumbi, K. A. Beyer, K. Chapman, D. A. Keen, T. D. Bennett and F. X. Coudert, *Nat. Mater.*, 2017, **16**, 1149–1155.

98 J. Zhang, S. H. Chai, Z. A. Qiao, S. M. Mahurin, J. Chen, Y. Fang, S. Wan, K. Nelson, P. Zhang and S. Dai, *Angew. Chemie - Int. Ed.*, 2015, **54**, 932–936.

99 L. Ma, C. J. E. Haynes, A. B. Grommet, A. Walczak, C. C. Parkins, C. M. Doherty, L. Longley, A. Tron, A. R. Stefankiewicz, T. D. Bennett and J. R. Nitschke, *Nat. Chem.*, 2020, **12**, 1–6.

100 T. A. Robbins, C. B. Knobler, D. R. Bellew and D. J. Cram, *J. Am. Chem. Soc.*, 1994, **116**, 111–122.

101 S. C. N. Hsu, M. Ramesh, J. H. Espenson and T. B. Rauchfus, *Angew. Chemie - Int. Ed.*, 2003, **42**, 2663–2666.

102 S. Vainberg, K. McClay, H. Masuda, D. Root, C. Condee, G. J. Zylstra and R. J. Steffan, *Appl. Environ. Microbiol.*, 2006, **72**, 5218–5224.

103 H. Liu, B. Liu, L. C. Lin, G. Chen, Y. Wu, J. Wang, X. Gao, Y. Lv, Y. Pan, X. Zhang, X. Zhang, L. Yang, C. Sun, B. Smit and W. Wang, *Nat. Commun.*, 2014, **5**, 1–7.

104 M. Costa Gomes, L. Pison, C. Červinka and A. Padua, *Angew. Chemie - Int. Ed.*, 2018, **57**, 11909–11912.

105 W. Shan, P. F. Fulvio, L. Kong, J. A. Schott, C. L. Do-Thanh, T. Tian, X. Hu, S. M. Mahurin, H. Xing and S. Dai, *ACS Appl. Mater. Interfaces*, 2018, **10**, 32–36.

106 J. Cahir, M. Y. Tsang, B. Lai, D. Hughes, M. A. Alam, J. Jacquemin, D. Rooney and S. L. James, *Chem. Sci.*, 2020, 2077–2084.

107 C. Zhang, R. S. Patil, T. Li, C. L. Barnes and J. L. Atwood, *Chem. Commun.*, 2017, **53**, 4312–4314.

108 H. Kumari, S. R. Kline, N. J. Schuster and J. L. Atwood, *Chem. Commun.*, 2011, **47**, 12298–12300.

109 N. P. Power, S. J. Dalgarno and J. L. Atwood, *New J. Chem.*, 2007, **31**, 17–20.

110 A. Bondi, *J. Phys. Chem.*, 1964, **68**, 441–451.

111 R. M. Mckinlay, P. K. Thallapally, G. W. V Cave and J. L. Atwood, *Angew. Chemie - Int. Ed.*, 2005, **117**, 5879–5882.

112 C. R. Pfeiffer, D. A. Fowler, S. Teat and J. L. Atwood, *CrystEngComm*, 2014, **16**, 10760–10773.

113 C. R. Pfeiffer, D. A. Fowler and J. L. Atwood, *CrystEngComm*, 2015, **17**, 4475–4485.

114 C. R. Pfeiffer, D. A. Fowler and J. L. Atwood, *Cryst. Growth Des.*, 2014, **14**, 4205–4213.

115 Cho, Rudkevich, Shivanyuk, Rissanen and Rebek, *Chemistry*, 2000, **6**, 3788–96.

116 D. Braga, F. Grepioni and J. J. Novoa, *Chem. Commun.*, 1998, **2**, 1959–1960.

117 J. Yang, B. Hong, N. Wang, X. Li, X. Huang, Y. Bao, C. Xie and H. Hao, *CrystEngComm*, 2019, **21**, 6374–6381.

118 R. M. McKinlay, G. W. V. Cave and J. L. Atwood, *Proc. Natl. Acad. Sci. U. S. A.*, 2005, **102**, 5944–5948.

119 R. Evans, Z. Deng, A. K. Rogerson, A. S. McLachlan, J. J. Richards, M. Nilsson and G. A. Morris, *Angew. Chemie - Int. Ed.*, 2013, **52**, 3199–3202.

120 N. Stock and S. Biswas, *Chem. Rev.*, 2012, **112**, 933–969.

121 L. Sciortino, A. Alessi, F. Messina, G. Buscarino and F. M. Gelardi, *J. Phys. Chem. C*, 2015, **119**, 7826–7830.

122 X. Hu, X. Lou, C. Li, Y. Ning, Y. Liao, Q. Chen, E. S. Mananga, M. Shen and B. Hu, *RSC Adv.*, 2016, **6**, 114483–114490.

123 M. Sanchez-Sanchez, I. De Asua, D. Ruano and K. Diaz, *Cryst. Growth Des.*, 2015, **15**, 4498–4506.

124 Q. Zhang, W. Wu, B. Xin and C. Li, *J. Chem. Technol. Biotechnol.*, 2007, **82**, 196–204.

125 T. Gerkensmeier, W. Iwanek, C. Agena, R. Fröhlich, S. Kotila, C. Näther and J. Mattay, *Eur. J. Org. Chem.*, 1999, 2257–2262.

126 C. Zhang, R. S. Patil, T. Li, C. L. Barnes and J. L. Atwood, *ChemComm*, 2017, **47**, 7634–7639.